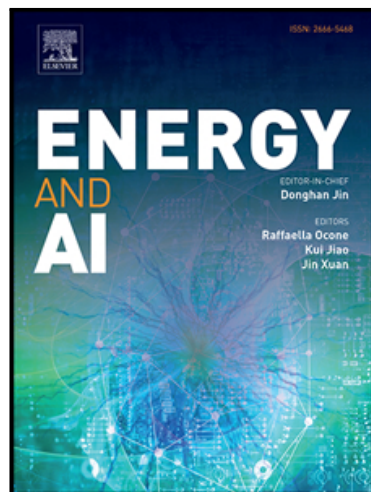


# Journal Pre-proof

Multi-Objective Performance Optimization & Thermodynamic Analysis of Solar Powered Supercritical CO<sub>2</sub> Power Cycles Using Machine Learning Methods & Genetic Algorithm

Asif Iqbal Turja , Md Mahmudul Hasan , M Monjurul Ehsan , Yasin Khan

PII: S2666-5468(23)00099-X  
DOI: <https://doi.org/10.1016/j.egyai.2023.100327>  
Reference: EGYAI 100327



To appear in: *Energy and AI*

Received date: 7 August 2023  
Revised date: 22 October 2023  
Accepted date: 2 December 2023

Please cite this article as: Asif Iqbal Turja , Md Mahmudul Hasan , M Monjurul Ehsan , Yasin Khan , Multi-Objective Performance Optimization & Thermodynamic Analysis of Solar Powered Supercritical CO<sub>2</sub> Power Cycles Using Machine Learning Methods & Genetic Algorithm, *Energy and AI* (2023), doi: <https://doi.org/10.1016/j.egyai.2023.100327>

This is a PDF file of an article that has undergone enhancements after acceptance, such as the addition of a cover page and metadata, and formatting for readability, but it is not yet the definitive version of record. This version will undergo additional copyediting, typesetting and review before it is published in its final form, but we are providing this version to give early visibility of the article. Please note that, during the production process, errors may be discovered which could affect the content, and all legal disclaimers that apply to the journal pertain.

© 2023 Published by Elsevier Ltd.  
This is an open access article under the CC BY-NC-ND license  
(<http://creativecommons.org/licenses/by-nc-nd/4.0/>)

## Highlights

- Investigated CSP integrated sCO<sub>2</sub> Brayton cycles' thermal performance and optimization
- Analysed solar irradiance's and climate temperature impact on the system extensively
- Explored TES dynamic operation at night and seasonal power generation patterns.
- Utilized a hybrid approach: machine learning with genetic algorithm for optimization.
- Achieved 16.985 MW power and 54.708% thermal efficiency with optimized condition

Journal Pre-proof

## **Multi-Objective Performance Optimization & Thermodynamic Analysis of Solar Powered Supercritical CO<sub>2</sub> Power Cycles Using Machine Learning Methods & Genetic Algorithm**

Asif Iqbal Turja, Md Mahmudul Hasan, M Monjurul Ehsan\*, Yasin Khan

Department of Mechanical and Production Engineering (MPE), Islamic University of Technology (IUT), Board Bazar, Gazipur-1704, Bangladesh

### **Abstract**

The present study is focused on multi-objective performance optimization & thermodynamic analysis from the perspectives of energy and exergy for Recompression, Partial Cooling & Main Compression Intercooling supercritical CO<sub>2</sub> (sCO<sub>2</sub>) Brayton cycles for concentrated solar power (CSP) applications using machine learning algorithms. The novelty of this work lies in the integration of artificial neural networks (ANN) and genetic algorithms (GA) for optimizing the performance of advanced sCO<sub>2</sub> power cycles considering climatic variation, which has significant implications for both the scientific community and engineering applications in the renewable energy sector. The methodology employed includes thermodynamic analysis based on energy, exergy & environmental factors including system performance optimization. The system is modelled for net power production of 15 MW thermal output utilizing equations for the energy and exergy balance for each component. Subsequently, thermodynamic model extracted dataset used for prediction & evaluation of Random Forest, XGBoost, KNN, AdaBoost, ANN and LightGBM algorithm. Finally, considering climate conditions, multi-objective optimization is carried out for the CSP integrated sCO<sub>2</sub> Power cycle for optimal power output, exergy destruction, thermal and exergetic efficiency. Genetic algorithm and TOPSIS (technique for order of preference by similarity to ideal solution), multi-objective decision-making tool, were used to determine the optimum operating conditions. The major findings of this work reveal significant improvements in the performance of the advanced sCO<sub>2</sub> cycle by 1.68% and 7.87% compared to conventional recompression and partial cooling cycle, respectively. This research could advance renewable energy technologies, particularly concentrated solar power, by improving power cycle designs to increase system efficiency and economic feasibility. Optimized advanced supercritical CO<sub>2</sub> power cycles in concentrated solar power plants might increase renewable energy use and energy generation infrastructure, potentially opening new research avenues.

### **Keywords**

Supercritical CO<sub>2</sub>; Concentrated solar power; Thermodynamic analysis; Machine Learning; Artificial Neural Network; Multi-objective optimization.

\*Corresponding Author: M Monjurul Ehsan ([ehsan@iut-dhaka.edu](mailto:ehsan@iut-dhaka.edu))

### **Nomenclature**

$A$	area, m <sup>2</sup>
$C_p$	specific heat at constant pressure, J/kg K

$E$	exergy, kW
$h$	specific enthalpy, kJ/kg
$\dot{m}$	mass flow rate, kg/s
$P$	pressure, MPa
$Q$	heat capacity, kW
$s$	specific entropy, kJ/kg K
$T$	temperature, °C or K
$W$	power output, MW
$x$	split ratio

**Greek symbols**

$\varepsilon$	recuperator effectiveness
$\eta$	Efficiency

**Subscripts**

$cyc$	cycle
$cos$	cosine
$ex$	exergy
$hel$	heliostat
$in$	inlet
$net$	net power
$out$	outlet
$rec$	receiver
$ref$	reflectivity
$s$	supercritical
$s\&h$	shading & blocking
$0$	environment state
$1, 2, 3, \dots$	state points

**Abbreviations**

ANN	artificial neural network
CSP	concentrated solar power
DP	design point
DNI	direct normal irradiance
DT	decision tree
GA	genetic algorithm
H	heater
HTR	high temperature recuperator
INT	main compression intercooling cycle
ICL	intercooler
KNN	k-nearest neighbor
LGBM	light gradient boosting machine
LTR	low temperature recuperator
MCIT	main compressor inlet temperature

MC	main compressor
ML	machine learning
MSE	mean square error
PAR	partial cooling cycle
PC	pre-compressor
PCL	pre-cooler
RC	recompressor
REC	recompression cycle
RF	random forest
RH	reheater
RMSE	root mean square error
RPR	ratio of pressure ratios
$R^2$	coefficient of determination
sCO <sub>2</sub>	supercritical carbon dioxide
sCO <sub>2</sub> BC	supercritical carbon dioxide Brayton cycle
TES	thermal energy storage
TIT	turbine inlet temperature
TOPSIS	technique for order preference by similarity to ideal solution
XGBoost	extreme gradient boosting

## 1. Introduction

In the current context of the energy and environmental challenges, it is imperative to enhance the effectiveness as well as affordability of energy conversion systems. Environmentalists have expressed long-standing concerns regarding climate change and the depletion of the ozone layer due to their potential threats to the sustainability of ecosystems [1]. In response to the increasing per capita energy demands, the global energy sectors are actively engaged in the progression and improvement of clean and efficient power production systems. The Supercritical CO<sub>2</sub> Brayton cycle (sCO<sub>2</sub>BC) has garnered significant attention due to its high thermodynamic efficiency. The Brayton cycle's operating fluid reaches the turbine at an extremely high temperature after receiving heat from the source, contributing to the high efficiency of the energy system [2]. The petroleum industry, mining processes, concentrating solar systems, electricity generation, waste heat recovery, geothermal power, nuclear power, and fossil fuels are only a few industries and energy applications where the sCO<sub>2</sub> is utilized [3]. This technology exhibits distinctive benefits in concentrated solar power (CSP) as energy sources, in which thermal energy storage enables prolonged operation beyond sunset, thereby mitigating temperature fluctuations and presenting CSP plants as a feasible alternative for fulfilling energy requirements in desert regions [4]. This study presents a methodology that utilizes Machine Learning techniques to predict performance, conduct parametric analysis, and optimize results. Thermodynamic analysis and multi-objective optimization are carried on the sCO<sub>2</sub>BC system utilizing artificial neural network (ANN) and regression models. This approach enables performing optimization processes that are relatively simple, efficient, and accurate.

### 1.1 Superiority and Potential Benefits of sCO<sub>2</sub> cycles

Supercritical CO<sub>2</sub> Brayton cycles, including comparisons of simple, recompression, and partial cooling are described and compared by Besarati et al. [5]. The concept of a bottoming cycle refers to a thermodynamic process in which waste heat from an existing power generation system is used. To utilize heat as effectively as possible, Organic Rankine Cycles (ORC) are included into each design. In some setups, Efficiency levels over 50% are attainable with the sCO<sub>2</sub> Brayton cycle. When combined with an ORC, the recompression cycle has enhanced potential. Persichilli et al. [6] discovered that sCO<sub>2</sub> technology can replace steam in gas turbines to produce more power, reduce installation, maintenance, and operating costs, and lower life cycle cost of ownership by 10–20%. According to Ehsan et al. [7], sCO<sub>2</sub> technologies outperform heat recovery steam generators in industrial applications due to their higher energy density, smaller component size, higher efficiency, lower environmental impact, and ease of installation.



*Fig. 1. Application of supercritical CO<sub>2</sub> cycle.*

**Fig. 1** depicts solar thermal, geothermal, nuclear, fuel cell, waste heat recovery, and coal as heat sources for the application of supercritical CO<sub>2</sub> cycles. Combining the advantages of steam Rankine cycles and gas turbines is possible with supercritical CO<sub>2</sub> Brayton cycles. A greater turbine input temperature can be used without causing material issues because, compared to the steam Rankine cycle, the fluid is compressed in the incompressible region. Supercritical CO<sub>2</sub>, at the same temperature, which causes less corrosion comparing to steam, may increase turbine inlet temperature [8]. Because of the characteristics of the working fluid, sCO<sub>2</sub>BC have exceptional advantages over conventional thermodynamic systems [9]:

- Supercritical CO<sub>2</sub> has a lower compression coefficient than working fluids such as air and water which indicates the system requires to carry out less compression energy.
- Systems heat exchangers and turbomachinery and are compact and ten times smaller than a standard power plant while producing an equal amount of power due to the increased density of sCO<sub>2</sub> [10].

- The CO<sub>2</sub> critical pressure (7.38 MPa) must be exceeded to avoid air intrusion. This simplifies power conversion. Low condenser pressure allows gas into the steam cycle, necessitating complex purification systems.
- Dry cooling could be used to cool the system, potentially saving water since the critical temperature of CO<sub>2</sub> is near to the ambient temperature [11].
- Because of these advantages, sCO<sub>2</sub> power systems are growing in popularity in a range of application scenarios like solar energy, waste heat utilization [12] & nuclear power plants [13,14].

## 1.2 CSP Plant Integrated with sCO<sub>2</sub>

For a 25 MW CSP plant, Ehsan et al. [15] examined the operation and design of the dry cooling system. Reyes-Belmonte et al. [16] reported on a single-stage sCO<sub>2</sub>BC in recompression in central receiver CSP plants that has a great deal of potential because of its remarkable thermodynamic features. Solar field-using dense particle suspension (DPS) receivers are suitable for sCO<sub>2</sub> power cycles from their high temperatures and stability. The power cycle efficiency ranges from 43% to 49% at turbine inlet temperatures between 630°C and 680°C, with a performance threshold of 75% fraction split ratio. Osorio et al. [17] simulated the fluctuating behavior of a central receiver CSP technique under various variations in the seasons and investigated the impacts of variables like intermediate pressures, mass flow rate, recuperator effectiveness, and number of compression-expansion phases on cycle efficiency. Process efficiency improved by 0.7% points across all four seasons, while average net power output increased by 12.6%, 14.3%, 16.2%, and 15.5% in the winter, spring, summer, and autumn, respectively.

## 1.3 CSP Plant Equipped with Thermal Energy Storage

Thermal energy storage (TES) systems are essential for increasing energy efficiency and integrating renewable energy sources. CSP facilitates cost-effective dry cooling [18] and efficient TES through the conversion of solar energy into heat prior to generating electricity. Yu et al.[19] proposes universal TES models for thermal storage technologies using the aggregated parameter method. According to the findings, all three systems charging and discharging capabilities are comparable, and that the dynamic characteristics of steam discharge temperature vary with critical parameters. In contemporary cost-efficient configurations of CSP systems, a two-tank TES system and a steam accumulator are integrated. The exergetic efficiency of a system decreases when the discharge temperature falls below the system's charged state. To enhance the operational capabilities and reduce the limitations on outlet temperature for the straightforward implementation of TES utilizing enclosed phase change material (PCM). A hybrid thermal energy storage system design and operation is suggested by Ma et al. [20]. Its reduced unit cost and increased utility factor make it a preferable alternative for encapsulated PCM for a variety of outlet temperature constraints.

## 1.4 Machine Learning Implementation on Power Cycle

Siddique et al. [21] analyzed five machine learning algorithms for Combined Cycle Power plant (CCPP) net power prediction using a six-year data set. The dataset evaluates output power based on input parameters such as temperature, humidity, and pressure. Gradient boosted Regression Tree performs better than all others, with 450 trees having the lowest RMSE and AE. Tufekci et al. [22] demonstrated a feasible model for predicting a base load operated power output. The CCPP is utilizing the Bagging technique with the REPTree predictor to predict the following day's hourly energy production. Wang et al.

[23] introduced a new Machine Learning-based method for predicting and optimizing ORC performance. BPNN and SVR models provided accurate predictions, proving research feasibility and effectiveness. SVR improves cycle operating parameter and reverse prediction. The approach has replaced the thermodynamic optimization, making it more rapid, precise, and efficient.

### **1.5 Multi-Objective Performance Optimization**

Besarati et al. [24] describes a multi-objective genetic algorithm (NSGA II) for Pareto approach optimization of cycle outputs in combined Brayton and inverse Brayton cycles. Saeed et al. [25] enhances the efficiency of a C-shaped PCHE by optimizing the channel design. Processing of dataset is done to train ML regression models, and a trained regression model is combined with a GA to determine the optimum set of design variables. For heat source conditions with variable temperature, Jin et al. [26] present an irreversible system and an ANN model for cycle performance optimization and assessment. Following the completion of the nonlinear ML model training and generalization, the systems and energy efficiencies are increased by changing the geometrical input variables. In science and engineering, it resolves multivariable problems. Similar to a chromosome in GA, each solution in particle swarm optimization (PSO) is represented by an avian. When it comes to analyzing cycle performance, Shannon Entropy is far superior; however, TOPSIS or LINMAP methods are more appropriate for making decisions.

### **1.6 Research Scope & Problem Statement**

The key contribution of this study involves thorough examination of the optimal MCIT, TIT, and climate conditions for sCO<sub>2</sub> Brayton cycles and optimization using advanced optimization framework to attain optimal thermal performance of the system. This analysis is conducted by employing machine learning algorithms and a creative approach to optimization using the Genetic Algorithm (GA) method. In addition to the comprehensive analysis and parametric optimization, this study also underscores the critical role of hyperparameter optimization for the machine learning algorithms, specifically the Artificial Neural Network (ANN), ensuring their optimal performance in modeling and optimization tasks. This study examines the optimization technique of sCO<sub>2</sub>BC, which incorporates concentrated solar power (CSP) and utilizes solar irradiance as the major source of heat. This study examines the impact of several factors on net power output, cycle thermal efficiency, and net energy utilization. The system design and performance are significantly influenced by climate conditions. Furthermore, an investigation has been performed for potential application of a Pre-compressor inside a recompression cycle, specifically in the context of partial cooling and main compression intercooling sCO<sub>2</sub>BC. This investigation also explores the inclusion of an additional cooler to enhance cooling at intermediate pressure, hence improving overall system performance. The scope of this work is outlined in the section below:

- Physical state reconstruction and thermodynamic characteristic prediction for three different sCO<sub>2</sub> power cycles (recompression, partial cooling and main compression intercooling cycle) validate the framework.
- The MCIT design-point at different temperatures is determined depending on the year-round ambient temperature profile to develop systems for distinct situations. Based on optimal MCIT conditions, the temperature of the hot & cold tank, and heliostat field design of TES are evaluated.

- The contribution of TES at night and its resulting patterns in power generation are shown for each season (summer, winter, autumn, and spring).
- To facilitate the DNI variation calculation, GA was used to optimize the variables to acquire the optimal design of the overall system & customized algorithmic strategies are created to reduce model complexity and accelerate model convergence.
- Extensive analysis and parametric optimization are performed to determine the effects of solar irradiance on the efficiency of the system.

## 2. System Description

**Fig. 2** depicts a schematic diagram of Recompression sCO<sub>2</sub>BC equipped with molten salt loop, which is considered as the base of this study. The Simple Brayton recuperation cycle has a pinch point issue, which reduces cycle efficiency, since the hot and cold fluid streams have different heat capacities. To solve this problem, the recompression cycle also includes LTR and the recompression compressor [27]. The recompression compressors receive a fraction of total mass flow rate of sCO<sub>2</sub> [28]. The recompression cycle lowers mass flow through the stream at high pressure. Consequently, the low-pressure stream is split after the low-temperature recuperator and compressed in the precooler and main compressor. **Fig. 3** shows the *T-s* diagram of Recompression sCO<sub>2</sub> cycle.

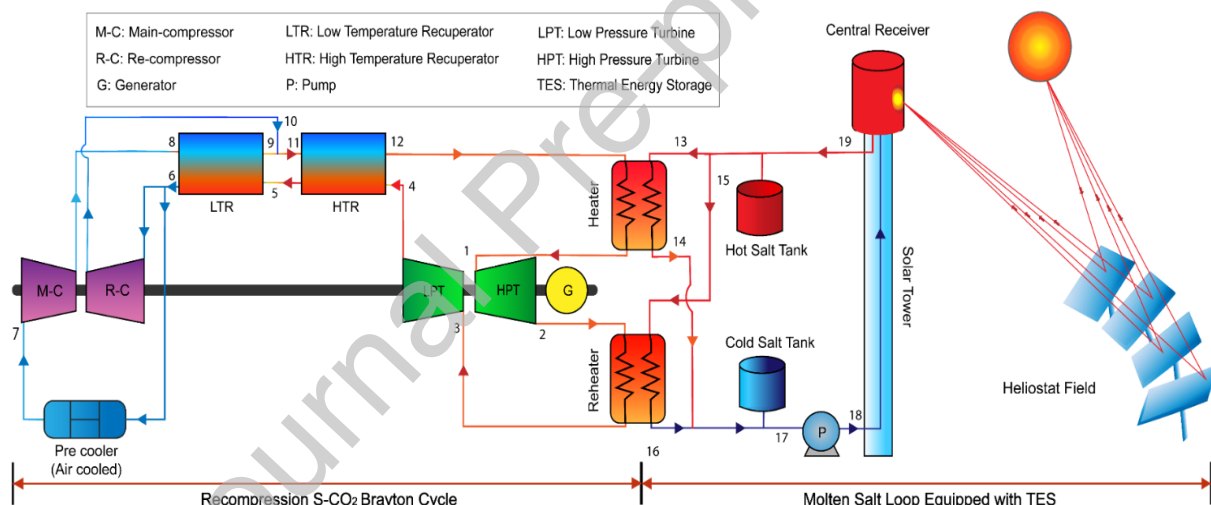


**Fig. 2.** Schematic diagram of Recompression sCO<sub>2</sub> cycle equipped with TES.

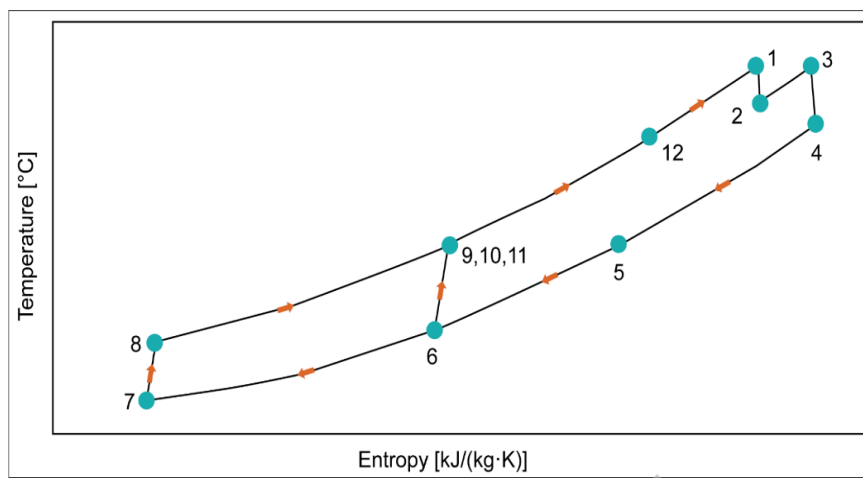


**Fig. 3.** T-s diagram of Recompression  $s\text{CO}_2$  cycle.

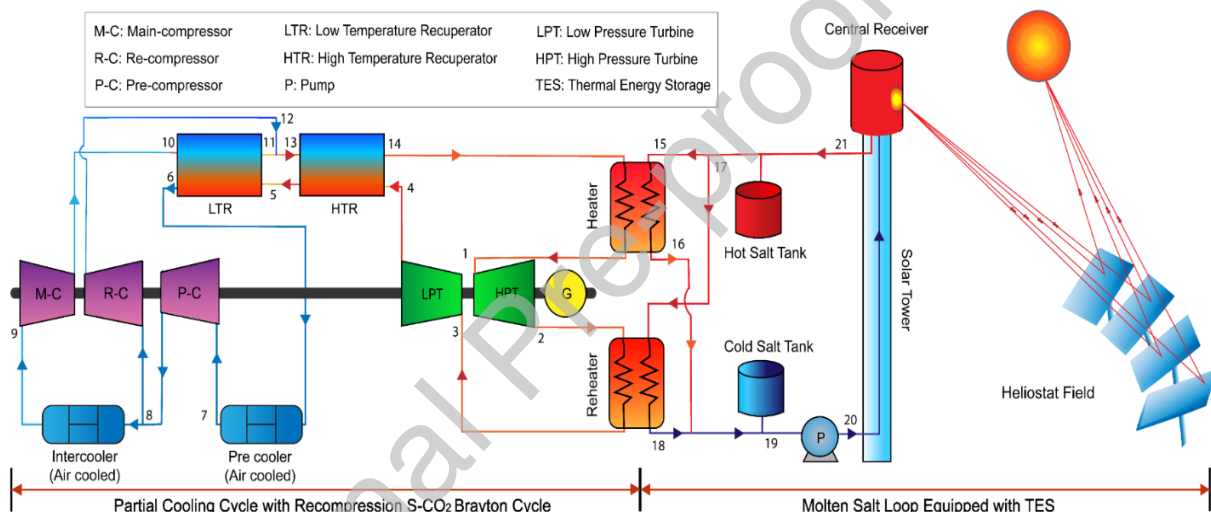


**Fig. 4.** Schematic diagram of Partial cooling  $s\text{CO}_2$  cycle equipped with TES.

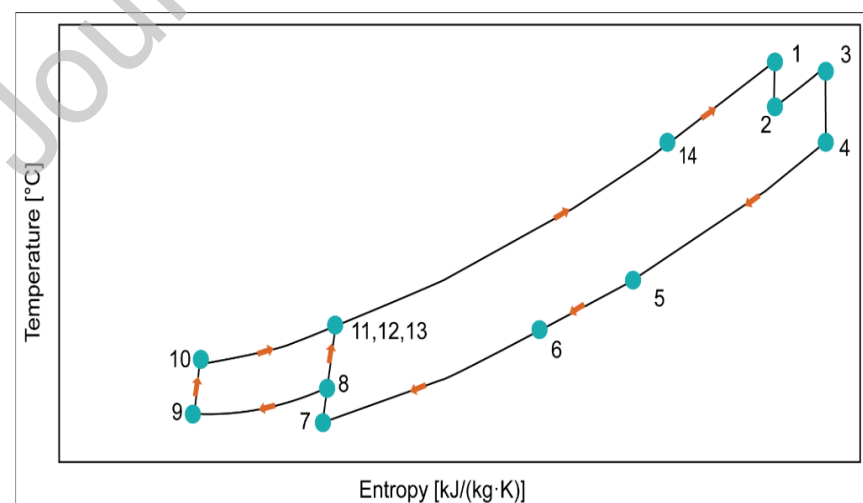


**Fig. 5.** T-s diagram of Partial cooling  $s\text{CO}_2$  cycle.

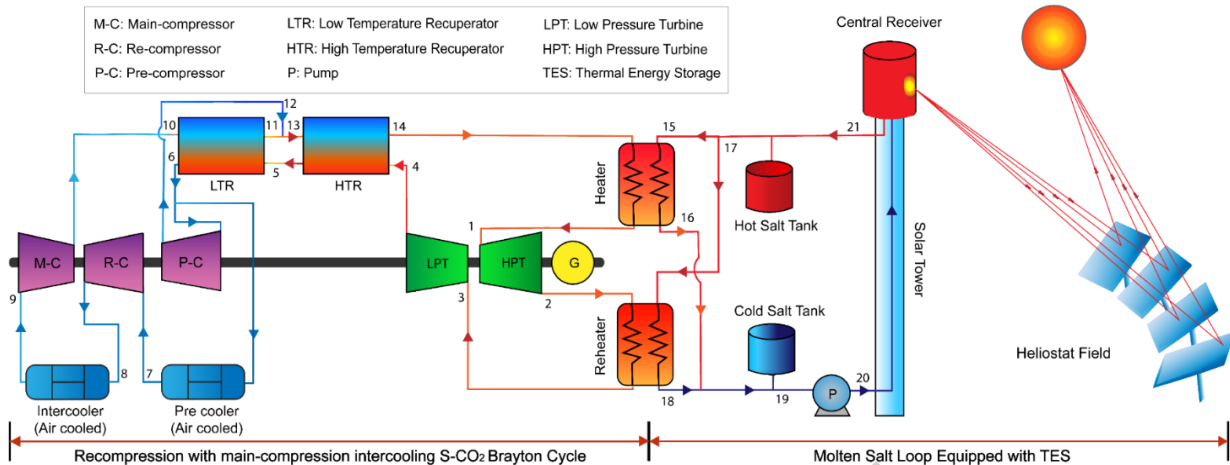


**Fig. 6.** Schematic diagram of Main-compression intercooling sCO<sub>2</sub> cycle equipped with TES.

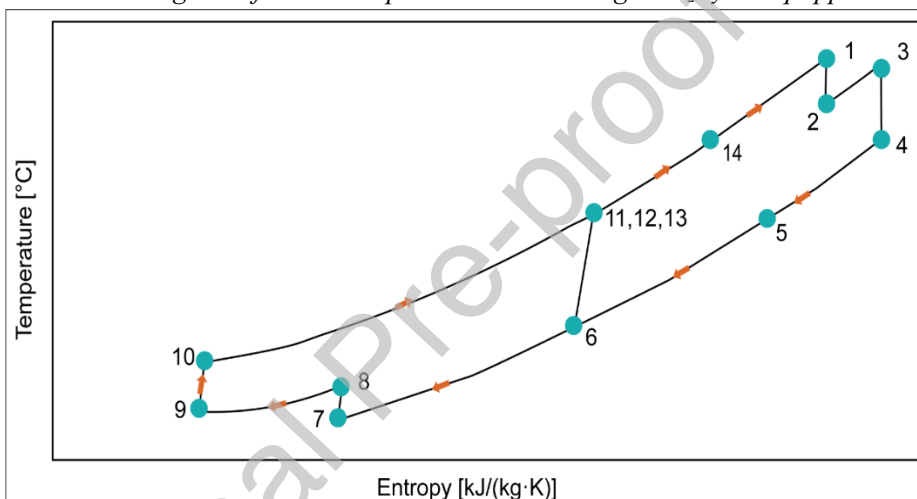


**Fig. 7.** T-s diagram of Main-compression intercooling sCO<sub>2</sub> cycle.

**Fig. 4** represents a modified recompression cycle by adding an extra compressor and an intercooler known as the partial cooling layout. The sCO<sub>2</sub> Simple Brayton cycle's efficiency can also be increased by partial cooling. The partial cooling cycle is analogous to the intercooling cycle in terms of the parts of the turbomachinery and the number of heat exchangers. A low-temperature recuperator's working fluid stream flows mostly in the precooler's direction during partial cooling [29]. The stream is split in a single possible intercooling recompression configuration following the pre-compressor [30]. Before it enters the pre-compressor, a precooler is used to cool the turbine exhaust flow. Thus, the pre-compressor's input pressure is intermediate, and the re-compressor contributes to the turbine pressure ratio [27]. **Fig. 5** shows the T-s diagram of partial cooling sCO<sub>2</sub> cycle.

**Table 1:** Description of the sCO<sub>2</sub> Brayton cycles.

Cycle	Compressor intercooling	Recuperators/ Turbines	Cooler	Compressor	Key Features
Recompression sCO <sub>2</sub> BC (REC)	No	HTR & LTR HPT & LPT	Precooler (Air-cooled)	Main Compressor, Re-compressor	<ul style="list-style-type: none"> <li>▪ Modified Simple Brayton cycle. An</li> <li>▪ An additional compressor is used.</li> <li>▪ Splitting the LTR's hot steam</li> </ul>

					reduces the cold stream's heat capacity.
Partial Cooling sCO <sub>2</sub> BC (PAR)	Yes	HTR & LTR HPT & LPT	Precooler (Air-cooled), Intercooler (Air-cooled)	Main Compressor, Re-compressor, and Pre-compressor	<ul style="list-style-type: none"> <li>▪ Modified REC sCO<sub>2</sub> Brayton cycle.</li> <li>▪ Pre-compressor is utilized in this configuration.</li> <li>▪ Splitting the stream exiting the main compressor reduces the cold stream's heat capacity.</li> <li>▪ To minimize compressor input power, an intercooling phase is added to the split fraction sent to the LTR.</li> </ul>
Main Compression Intercooling sCO <sub>2</sub> BC (INT)	Yes	HTR & LTR HPT & LPT	Precooler (Air-cooled), Intercooler (Air-cooled)	Main Compressor, Re-compressor, and Pre-compressor	<ul style="list-style-type: none"> <li>▪ A modified PAR sCO<sub>2</sub> Brayton cycle.</li> <li>▪ After the MC is introduced, an intercooling step is added to lower the power input to the compressors.</li> </ul>

In **Fig. 6**, the schematic diagram of Main-compression intercooling sCO<sub>2</sub> cycle is presented. In main-compression intercooling cycle, two intercooling stages are separated from the primary compressor. The main compressor gets working fluid at high pressure and temperature. Before entering the main compressor, the stream from the precooler flows via an intercooling stage and a low-pressure compressor. Since the compressor input temperature significantly affects system performance, cooling system design is crucial [31]. In this configuration, the re-compressor operates over the entire pressure ratio since the inlet pressure is at the turbine outlet pressure [27]. What unites them is the idea that both the intercooling cycle and the recompression cycle involve multistage compression with intercooling [32]. **Fig. 7** shows the *T-s* diagram of Main Compression Intercooling sCO<sub>2</sub> cycle.

All heat exchangers and devices (compressors and turbines) are mass, energy, and exergy balanced for the thermodynamic study of the sCO<sub>2</sub>BC designs. An effectiveness factor for the whole hot stream was taken into account for setups with the LTR, and the HTR is simulated through presuming the effectiveness of a heat exchanger [5]. In sCO<sub>2</sub>BC with LTR, split ratio is the ratio of the sCO<sub>2</sub>'s total mass flow rate to the cold stream's mass flow rate. Split ratio is calculated from the LTR's energy balance, which is used to compute thermal performance and compression power. **Table 1** demonstrates the key features of three sCO<sub>2</sub>BC layouts.

### 3. Research Methodology

#### 3.1 Assumptions

The first and second laws of thermodynamics are applied to the different devices under analysis to create a mathematical model of the 3 layouts of sCO<sub>2</sub> Brayton cycles. Python programming is used to execute the simulation. The primary presumptions made in order to streamline the simulation of the system are as follows:

- The steady-state condition is considered to be attained by all three cycles.
- Except for the solar field components, there are negligible heat losses from the cycle components to the ambient air.
- A 360° external cylinder receiver is used to collect more of the light that is reflected from the edge of the solar field.

- All heat recuperators and pipelines ignore pressure drops and friction losses.
- The system's kinetic and potential energy hardly change over time.
- Solar salt split ratio to thermal energy storage is considered 0.5 for molten salt loop.
- For the two primary compression stages, it is assumed that the input temperatures are the same.

### 3.2 Energy Analysis

In this article, recompression, partial cooling & main-compression intercooling sCO<sub>2</sub>BC configurations coupled with CSP loop are utilized in order to examine the performance under off-design conditions. When analyzing all of the components, both energy and mass conservation principles from the first law of thermodynamics was utilized. Ratio of pressure ratios, net work output & cycle thermal efficiency can be calculated using Equations (1)-(3).

$$\text{Ratio of pressure ratios[27]} , RPR = \frac{\frac{P_{high}}{P_{intermediate}} - 1}{\frac{P_{high}}{P_{low}} - 1} \quad (1)$$

$$\text{Net work output, } \dot{W}_{net} = \dot{W}_T - \dot{W}_P \quad (2)$$

$$\text{Thermal efficiency of the cycle, } n_{cyc} = \frac{\dot{W}_{net}}{Q_H} \quad (3)$$

The energy equation of each component for 3 layouts of sCO<sub>2</sub> cycles are presented in **Table 2**, **Table 3**, and **Table 4**.

**Table 2:** Components-wise energy equation of recompression cycle.

Component	Equation
Compressor isentropic efficiency	$n_c = \frac{h_{8,s} - h_7}{h_8 - h_7}$
Turbine isentropic efficiency	$n_T = \frac{h_1 - h_2}{h_1 - h_{2,s}}$
Work input to the compressor	$\dot{W}_C = \dot{m}_{CO_2} (h_8 - h_7)$
Work output from the turbine	$\dot{W}_T = \dot{m}_{CO_2} (h_4 - h_5)$
Heat input by the heater	$Q_H = \dot{m}_{CO_2} (h_1 - h_{12})$
Recuperator effectiveness	$\varepsilon_R = \frac{\dot{m}_{CO_2} (h_4 - h_5)}{Q_{max}}$
Split ratio	$SR = \frac{\dot{m}_9}{\dot{m}_9 + \dot{m}_{10}}$

**Table 3:** Components-wise energy equation of partial cooling cycle.

Component	Equation
Main Compressor isentropic efficiency	$n_c = \frac{h_{10,s} - h_9}{h_{10} - h_9}$
Turbine isentropic efficiency	$n_T = \frac{h_1 - h_2}{h_1 - h_{2,s}}$

Work input to the compressor	$\dot{W}_C = \dot{m}_{CO_2} (h_{10} - h_9)$
Work output from the turbine	$\dot{W}_T = \dot{m}_{CO_2} (h_4 - h_5)$
Heat input by the heater	$Q_H = \dot{m}_{CO_2} (h_1 - h_{14})$
Recuperator effectiveness	$\varepsilon_R = \frac{\dot{m}_{CO_2} (h_4 - h_5)}{Q_{max}}$
Split ratio	$SR = \frac{\dot{m}_{11}}{\dot{m}_{11} + \dot{m}_{12}}$

**Table 4:** Components-wise energy equation of main compression intercooling cycle.

Component	Equation
Main Compressor isentropic efficiency	$n_C = \frac{h_{10,s} - h_9}{h_{10} - h_9}$
Turbine isentropic efficiency	$n_T = \frac{h_1 - h_2}{h_1 - h_{2,s}}$
Work input to the compressor	$\dot{W}_C = \dot{m}_{CO_2} (h_{10} - h_9)$
Work output from the turbine	$\dot{W}_T = \dot{m}_{CO_2} (h_4 - h_5)$
Heat input by the heater	$Q_H = \dot{m}_{CO_2} (h_1 - h_{14})$
Recuperator effectiveness	$\varepsilon_R = \frac{\dot{m}_{CO_2} (h_4 - h_5)}{Q_{max}}$
Split ratio	$SR = \frac{\dot{m}_{11}}{\dot{m}_{11} + \dot{m}_{12}}$

**Table 5:** CSP field and TES equations.

Parameter	Equation
Heliostat field efficiency [33]	$\eta_{s\&b} \cdot \eta_{int} \cdot \eta_{att} \cdot \eta_{ref}$
Solar receiver heat input [33]	$\dot{Q}_{rec,in} = \eta_{cos} \cdot \dot{Q}_{sun} = \eta_{field} \cdot (DNI) \cdot A_{hel} \cdot N_{hel}$
Solar receiver efficiency [33]	$\eta_{rec} = \frac{\dot{Q}_{rec,net}}{\dot{Q}_{rec,in}}$
Heliostat field efficiency [33]	$\eta_{cos} \cdot \eta_{s\&b} \cdot \eta_{int} \cdot \eta_{att} \cdot \eta_{ref}$
TES capacity ratio [34]	$\sigma = \frac{E_{stored}}{E_{max, stored}}$
Maximum theoretical storage capacity [34]	$E_{max, stored} = m_{pcm} c_{p,s} (T_{ain} - T_{bin}) + m_{pcm} L$

### 3.3 Exergy Analysis

Exergy may be defined as an energy stream's maximum work potential when compared to its surroundings. The exergy balance equation in a steady-state controlled volume system is presented as:

$$\dot{X}_{dest,i} = \sum(\dot{m}_{in} \times x_{in}) - \sum(\dot{m}_{out} \times x_{out}) + \sum \dot{Q} \times \left(1 - \frac{T_0}{T}\right)_{in} - \sum \dot{Q} \times \left(1 - \frac{T_0}{T}\right)_{out} + \sum \dot{W} \quad (04)$$

Where the term ‘ $x$ ’ refers to the exergy of an energy stream in a controlled volume steady-state system, which is defined as:

$$x_i = h_i - h_o - T_o \times (s_i - s_o) \quad (05)$$

The ratio of energy yield to energy input is used to determine the second law of efficiency. The exergetic efficiency of the entire cycle can be determined by:

$$\eta_{exergy} = (1 - \frac{\dot{X}_{dest}}{\dot{X}_{in}}) \quad (06)$$

Components-wise exergy destruction equation of each component for 3 layouts of sCO<sub>2</sub> cycles are demonstrated in **Table 6**, **Table 7**, and **Table 8**.

**Table 6:** Components-wise exergy destruction equation of recompression cycle.

Component	Equation
Heater	$X_H = \dot{m}_{CO_2}[(h_{12} - h_1) - T_0(s_{12} - s_1)] + \dot{m}_{CO_2}[1 - \left(\frac{T_0}{T_H}\right)]\dot{Q}_H$
Reheater	$X_{RH} = \dot{m}_{CO_2}[(h_2 - h_3) - T_0(s_2 - s_3)] + \dot{m}_{CO_2}[1 - \left(\frac{T_0}{T_{RH}}\right)]\dot{Q}_{RH}$
HTR	$X_{HTR} = \dot{m}_{CO_2}[(h_4 - h_5) - T_0(s_4 - s_5)] + \dot{m}_{CO_2}[(h_{10} - h_{12}) - T_0(s_{10} - s_{12})]$
LTR	$X_{LTR} = \dot{m}_{CO_2}[(h_5 - h_6) - T_0(s_5 - s_6)] + \dot{m}_{CO_2}(1 - SR)[(h_8 - h_{10}) - T_0(s_8 - s_{10})]$
Main compressor	$X_{MC} = SR \cdot \dot{m}_{CO_2}[(h_7 - h_8) - T_0(s_7 - s_8)] + W_{MC}$
Re-compressor	$X_{RC} = (1 - SR) \cdot \dot{m}_{CO_2}[(h_6 - h_{10}) - T_0(s_6 - s_{10})] + W_{RC}$
HPT	$X_{HPT} = \dot{m}_{CO_2}[(h_1 - h_2) - T_0(s_1 - s_2)] - W_{HPT}$
LPT	$X_{LPT} = \dot{m}_{CO_2}[(h_3 - h_4) - T_0(s_3 - s_4)] - W_{LPT}$
Pre-cooler	$X_{PCL} = SR \cdot \dot{m}_{CO_2}[(h_6 - h_7) - T_0(s_6 - s_7)]$
Exergy input	$X_{in} = \dot{m}_{CO_2}[1 - \left(\frac{T_0}{T_1}\right)]\dot{Q}_H + \dot{m}_{CO_2}[1 - \left(\frac{T_0}{T_3}\right)]\dot{Q}_{RH}$
Total Exergy destruction	$X_{dest} = X_H + X_{RH} + X_{HTR} + X_{LTR} + X_{MC} + X_{RC} + X_{HPT} + X_{LPT} + X_{PCL}$

**Table 7:** Components-wise exergy destruction equation of partial cooling cycle.

Component	Equation
Heater	$X_H = \dot{m}_{CO_2}[(h_{14} - h_1) - T_0(s_{14} - s_1)] + \dot{m}_{CO_2}[1 - \left(\frac{T_0}{T_H}\right)]\dot{Q}_H$
Reheater	$X_{RH} = \dot{m}_{CO_2}[(h_2 - h_3) - T_0(s_2 - s_3)] + \dot{m}_{CO_2}[1 - \left(\frac{T_0}{T_{RH}}\right)]\dot{Q}_{RH}$
HTR	$X_{HTR} = \dot{m}_{CO_2}[(h_4 - h_5) - T_0(s_4 - s_5)] + \dot{m}_{CO_2}[(h_{12} - h_{14}) - T_0(s_{12} - s_{14})]$

LTR	$X_{LTR} = \dot{m}_{CO_2}[(h_5 - h_6) - T_0(s_5 - s_6)] + \dot{m}_{CO_2}(1 - SR)[(h_{10} - h_{12}) - T_0(s_{10} - s_{12})]$
Main compressor	$X_{MC} = SR \cdot \dot{m}_{CO_2}[(h_9 - h_{10}) - T_0(s_9 - s_{10})] + W_{MC}$
Re-compressor	$X_{RC} = (1 - SR) \cdot \dot{m}_{CO_2}[(h_8 - h_{12}) - T_0(s_8 - s_{12})] + W_{RC}$
Pre-compressor	$X_{PC} = \dot{m}_{CO_2}[(h_7 - h_8) - T_0(s_7 - s_8)] + W_{PC}$
HPT	$X_{HPT} = \dot{m}_{CO_2}[(h_1 - h_2) - T_0(s_1 - s_2)] - W_{HPT}$
LPT	$X_{LPT} = \dot{m}_{CO_2}[(h_3 - h_4) - T_0(s_3 - s_4)] - W_{LPT}$
Pre-cooler	$X_{PCL} = \dot{m}_{CO_2}[(h_6 - h_7) - T_0(s_6 - s_7)]$
Intercooler	$X_{ICL} = SR \cdot \dot{m}_{CO_2}[(h_8 - h_9) - T_0(s_8 - s_9)]$
Exergy input	$X_{in} = \dot{m}_{CO_2}[1 - \left(\frac{T_0}{T_1}\right)] \dot{Q}_H + \dot{m}_{CO_2}[1 - \left(\frac{T_0}{T_3}\right)] \dot{Q}_{RH}$
Total Exergy destruction	$X_{dest} = X_H + X_{RH} + X_{HTR} + X_{LTR} + X_{MC} + X_{RC} + X_{PC} + X_{HPT} + X_{LPT} + X_{PCL} + X_{ICL}$

**Table 8:** Components-wise exergy destruction equation of main compression intercooling cycle.

Component	Equation
Heater	$X_H = \dot{m}_{CO_2}[(h_{14} - h_1) - T_0(s_{14} - s_1)] + \dot{m}_{CO_2}[1 - \left(\frac{T_0}{T_H}\right)] \dot{Q}_H$
Reheater	$X_{RH} = \dot{m}_{CO_2}[(h_2 - h_3) - T_0(s_2 - s_3)] + \dot{m}_{CO_2}[1 - \left(\frac{T_0}{T_{RH}}\right)] \dot{Q}_{RH}$
HTR	$X_{HTR} = \dot{m}_{CO_2}[(h_4 - h_5) - T_0(s_4 - s_5)] + \dot{m}_{CO_2}[(h_{12} - h_{14}) - T_0(s_{12} - s_{14})]$
LTR	$X_{LTR} = \dot{m}_{CO_2}[(h_5 - h_6) - T_0(s_5 - s_6)] + \dot{m}_{CO_2}(1 - SR)[(h_{10} - h_{12}) - T_0(s_{10} - s_{12})]$
Main compressor	$X_{MC} = SR \cdot \dot{m}_{CO_2}[(h_9 - h_{10}) - T_0(s_9 - s_{10})] + W_{MC}$
Re-compressor	$X_{RC} = (1 - SR) \cdot \dot{m}_{CO_2}[(h_6 - h_{12}) - T_0(s_6 - s_{12})] + W_{RC}$
Pre-compressor	$X_{PC} = \dot{m}_{CO_2}[(h_7 - h_8) - T_0(s_7 - s_8)] + W_{PC}$
HPT	$X_{HPT} = \dot{m}_{CO_2}[(h_1 - h_2) - T_0(s_1 - s_2)] - W_{HPT}$
LPT	$X_{LPT} = \dot{m}_{CO_2}[(h_3 - h_4) - T_0(s_3 - s_4)] - W_{LPT}$
Pre-cooler	$X_{PCL} = SR \cdot \dot{m}_{CO_2}[(h_6 - h_7) - T_0(s_6 - s_7)]$
Intercooler	$X_{ICL} = SR \cdot \dot{m}_{CO_2}[(h_8 - h_9) - T_0(s_8 - s_9)]$
Exergy input	$X_{in} = \dot{m}_{CO_2}[1 - \left(\frac{T_0}{T_1}\right)] \dot{Q}_H + \dot{m}_{CO_2}[1 - \left(\frac{T_0}{T_3}\right)] \dot{Q}_{RH}$
Total Exergy destruction	$X_{dest} = X_H + X_{RH} + X_{HTR} + X_{LTR} + X_{MC} + X_{RC} + X_{PC} + X_{HPT} + X_{LPT} + X_{PCL} + X_{ICL}$

### 3.4 Framework of the Mathematical Model

A simulation model is executed in the Python programming language using the equations for energy balance and exergy destruction. The integrated CoolProp library is used for obtaining sCO<sub>2</sub>'s properties. **Table 9** and **Table 10** shows the operational parameters that are taken into consideration for cycle simulation. The controllable variable ranges are selected from published literatures [35,36] that investigated the parametric impacts of variables on various configurations of the sCO<sub>2</sub> Brayton cycle.

**Fig. 8** depicts the simulation model's stages. In order to provide a thorough understanding of the effects of each controllable variable, graphs are generated by changing one controllable variable within the acceptable range while keeping the others constant. Weather data is utilized to analyze cycle performance on different seasons throughout a year. Multiple machine learning model performance have been compared to find best-fit model for this study. Additionally, using a genetic algorithm, multi-objective optimization has been performed to provide an ideal set of data for optimal cycle performance. The results of this research are graphically assessed in the following sections.

**Table 9:** Initial parameters for simulation and analysis of system performance.

Parameters	Values	Unit
Maximum pressure, $P_{max}$	25	MPa
Minimum pressure, $P_{min}$	8	MPa
Turbine inlet temperature, $TIT$	600	°C
Main compressor inlet temperature, $MCIT$	34	°C
Pinch temperature, $T_{pinch}$	7	°C
Mass flow rate of the sCO <sub>2</sub> cycle, $\dot{m}_{CO_2}$	1	kg/s
Effectiveness of HTR	0.97	-
Effectiveness of LTR	0.88	-
Compressor isentropic efficiency, $\eta_c$	0.89	-
Turbine isentropic efficiency, $\eta_t$	0.90	-

**Table 10:** CSP loop Design Parameters.

Parameters	Symbol	Values	Unit
Direct normal irradiance	$DNI$	0.6	kW/m <sup>2</sup>
Cosine effect efficiency	$\eta_{cos}$	0.8267	-
Shading and blocking efficiency	$\eta_{s\&b}$	0.9698	-
Interception efficiency	$\eta_{int}$	0.971	-
Atmospheric attenuation efficiency	$\eta_{att}$	0.9383	-
Reflectivity efficiency of heliostat	$\eta_{ref}$	0.88	-
Number of heliostats	$N_{hel}$	624	-
Reflective area of each heliostat	$A_{hel}$	$9.45 \times 12.84$	m <sup>2</sup>
Receiver aperture area	$A_{rec}$	68.1	m <sup>2</sup>

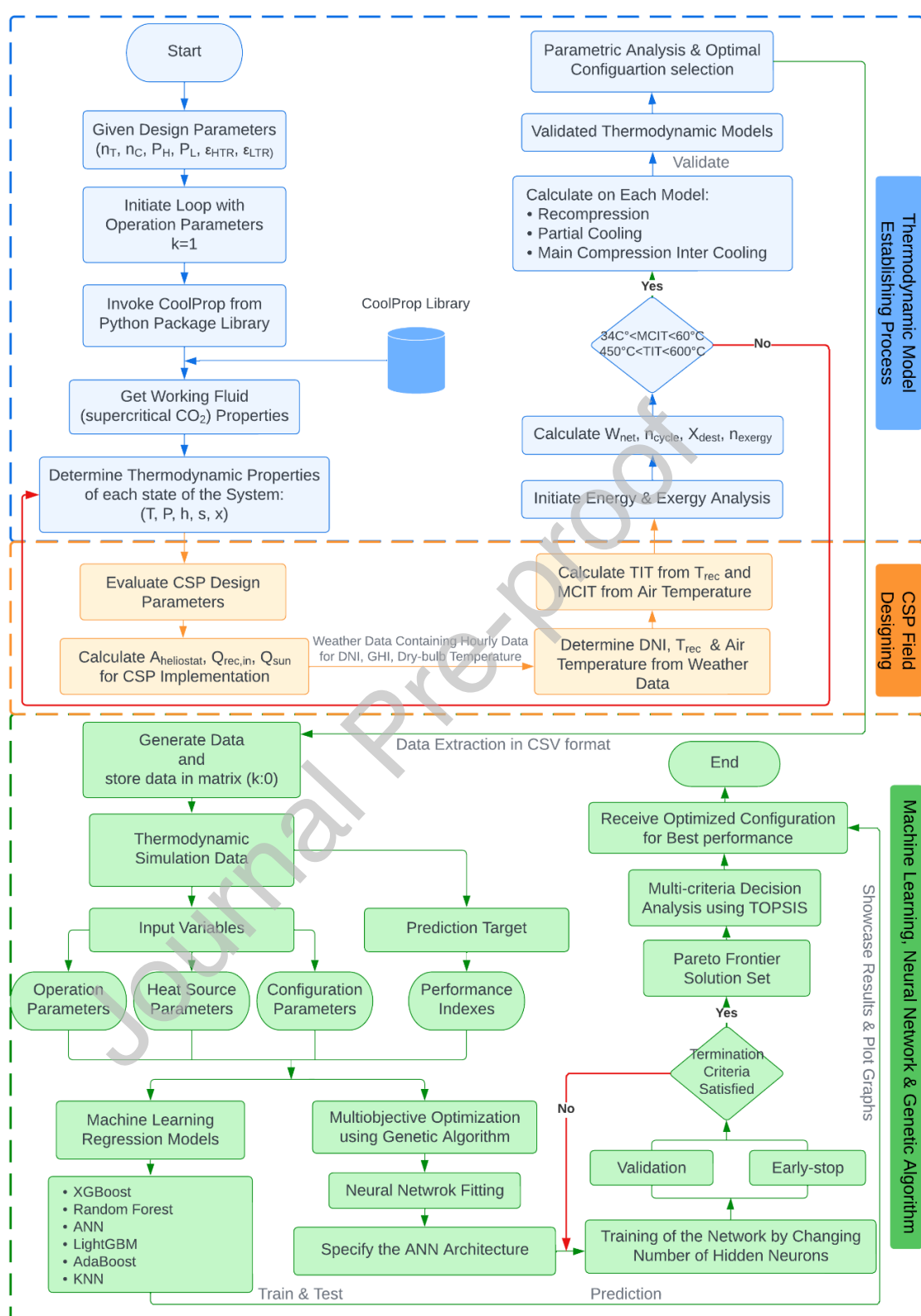


**Fig. 8.** Flow chart demonstrating cycle modelling, data extraction & performance optimization for sCO<sub>2</sub>BC.

### 3.5 Boundary Conditions

CoolProp library is utilized to determine the working fluid's thermal characteristics and each cycle's thermodynamic performance. The base model's initial conditions are illustrated in **Table 9** and **Table 10**. The results of this research are graphically assessed in the next section.

### 4. Model Validation

Earlier research from the literature has been used to verify the layout of recompression, partial cooling and main compression intercooling sCO<sub>2</sub> cycles. **Fig. 9** compares the cycle thermal efficiency obtained by the current model and from the previous data [27] for the variation of MCIT (45°C– 65°C) & TIT (500°C– 850°C). The figure exhibits very strong model agreement. Fig. 8 illustrates the entire model development process. **Table 11** demonstrates the boundary conditions at which the validation is performed.

**Table 11:** Cycle model validation boundary conditions.

Cycles	Turbine efficiency	Compressor efficiency	HTR effectiveness	LTR effectiveness	Pinch temperature	Maximum pressure	RPR	Pressure ratio
Recompression	93%	89%	97%	88%	5 K	25 MPa	-	2.7
Partial cooling	93%	89%	97%	88%	5 K	25 MPa	0.97	5.0
Main compression intercooling	93%	89%	97%	90%	5 K	25 MPa	0.60	3.6

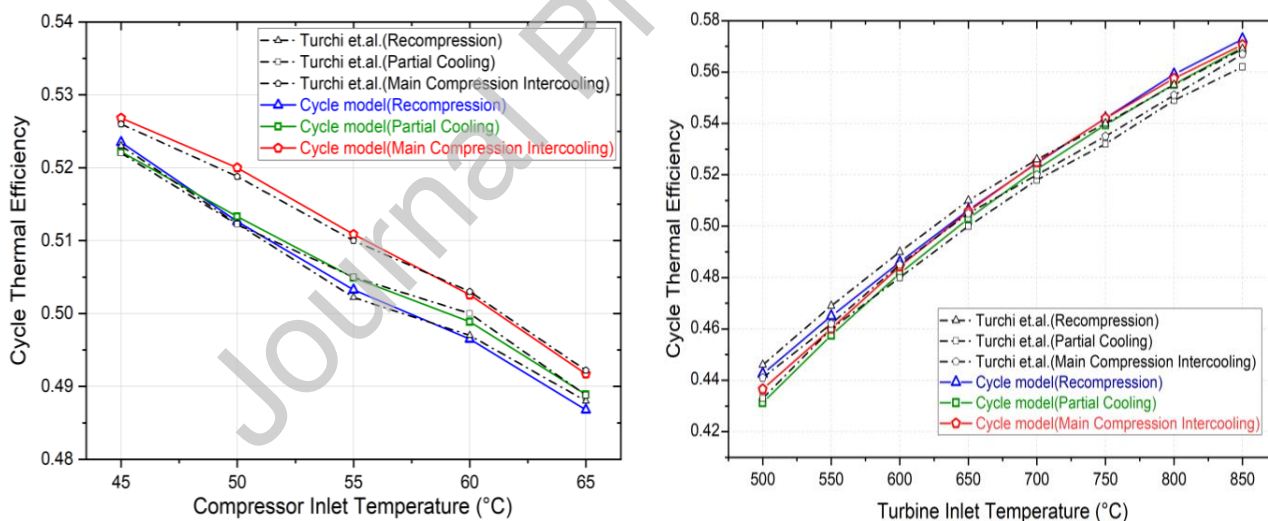


**Fig. 9.** Cycle model validation for MCIT & TIT variation.

### 5. Results and Discussion

#### 5.1 Thermodynamic Analysis

To illustrate the thermodynamic state attributes of recompression sCO<sub>2</sub>BC, **Table 12** is developed provided the cited configurations in **Table 9**. In addition, thermodynamic state properties for partial cooling & main-compression intercooling sCO<sub>2</sub>BC are displayed in **Table 13** and **Table 14**, respectively.

**Table 12:** Recompression sCO<sub>2</sub> cycle pressure, temperature, enthalpy & entropy for each state point.

State (i)	T (°C)	P (MPa)	h (kJ/kg)	s (kJ/kg·K)
1	600	25	1094.689	2.767
2	546.108	16.5	1032.902	2.775
3	600	16.5	1099.484	2.854
4	509.777	8	996.47	2.869
5	200.327	8	640.034	2.291
6	82.934	8	495.911	1.939
7	34	8	320.691	1.391
8	75.834	25	350.18	1.401
9	192.324	25	572.98	1.957
10	192.327	25	572.98	1.957
11	192.327	25	572.98	1.957
12	468.0952	25	929.416	2.562

**Table 13:** Partial cooling sCO<sub>2</sub> cycle pressure, temperature, enthalpy & entropy for each state point.

State (i)	T (°C)	P (MPa)	h (kJ/kg)	s (kJ/kg·K)
1	600	25	1094.689	2.767
2	544.433	16.5	30.842	2.773
3	600	16.5	1099.484	2.854
4	506.897	8	993.036	2.864
5	103.09	8	523.998	2.016
6	60.936	8	459.916	1.834
7	35	8	352.291	1.494
8	48.558	10.498	358.523	1.496
9	35	10.498	286.459	1.268
10	56.523	25	307.531	1.275
11	92.35	25	387.409	1.505
12	92.35	25	387.409	1.505
13	92.35	25	387.409	1.505
14	409.56	25	856.447	2.459

**Table 14:** Main Compression Intercooling sCO<sub>2</sub> cycle pressure, temperature, enthalpy & entropy for every state point.

State (i)	T (°C)	P (MPa)	h (kJ/kg)	s (kJ/kg·K)
1	600	25	1094.689	2.767
2	544.433	16.5	1030.842	2.773
3	600	16.5	1099.484	2.854
4	506.897	8	993.0367	2.864
5	178.593	8	615.201	2.237
6	64.746	8	446.908	1.855
7	34	8	320.691	1.391
8	43.582	10.5	325.598	1.393
9	34	10.5	282.898	1.256
10	54.746	25	303.707	1.263

11	168.462	25	534.376	1.872
12	168.462	25	534.376	1.872
13	168.462	25	534.376	1.872
14	454.293	25	912.211	2.538

## 5.2 Effect of TIT

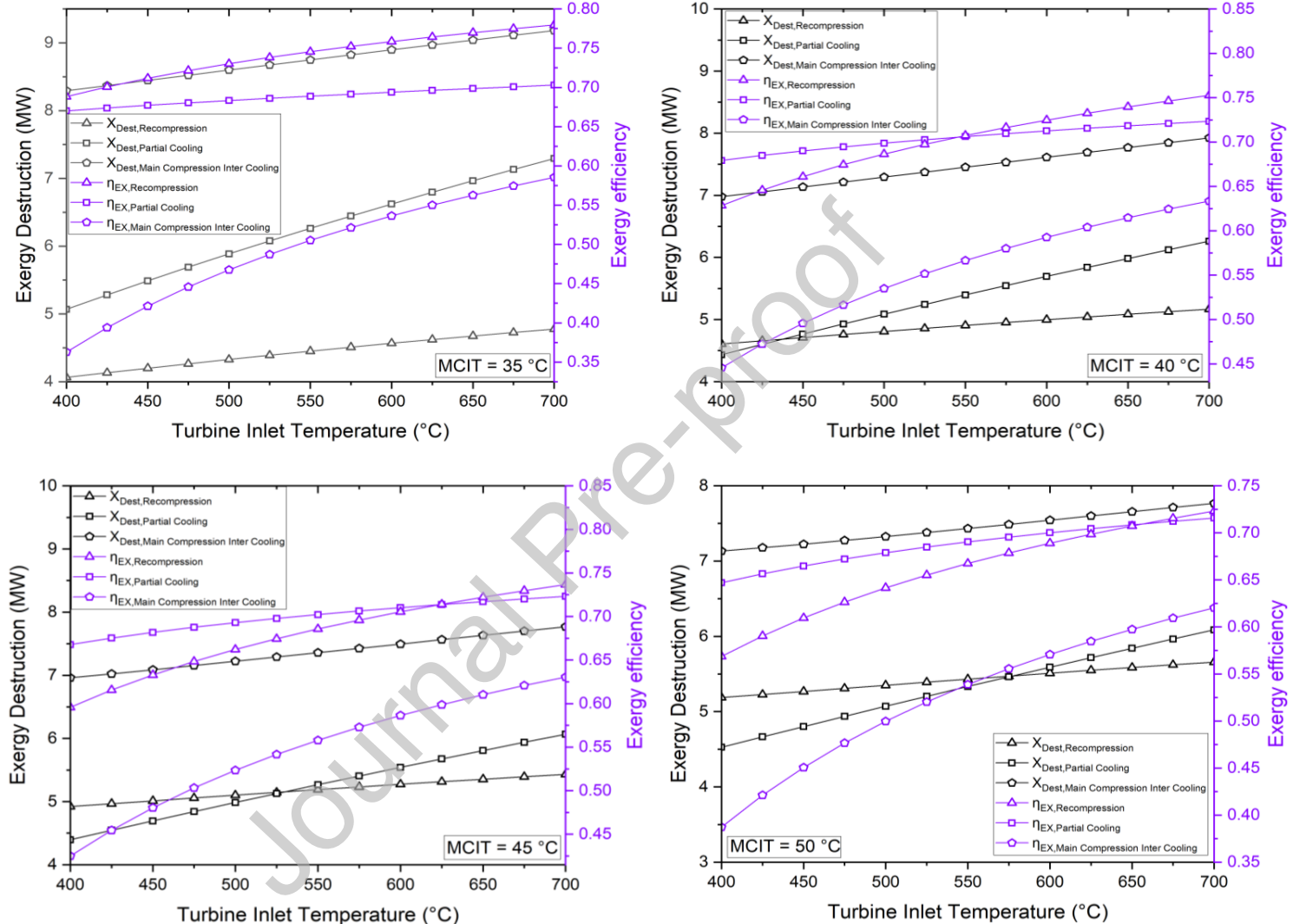


**Fig. 10.** Exergy destruction & exergy efficiency comparison for recompression, partial cooling & intercooling cycle with the variation of the TIT at different compressor inlet temperature of 35°C, 40°C, 45°C and 50°C.

According to previous studies and the laws of thermodynamics, increasing TIT causes the sCO<sub>2</sub> power cycles' thermal efficiency to increase. **Fig. 10** depicts exergy destruction & energetic efficiency comparison of all three cycle configurations with the changes in turbine inlet temperature. During the comparative analysis, the MCIT is maintained constant, while the TIT is systematically adjusted within the range of 400°C to 700°C. Based on this comparison, it can be seen that the recompression sCO<sub>2</sub>BC

exhibits better exergetic efficiency at lower MCIT values. Conversely, the partial cooling sCO<sub>2</sub>BC demonstrates better performance at higher MCIT circumstances. When MCIT  $\geq 45^\circ\text{C}$ , there is noticeable rise in the amount of exergy destruction occurring within the recompression cycle. Nevertheless, the influence of this rise on the trend of increasing TIT is rather insignificant. Observable differences in efficiency can be observed when intercooling is employed in the main compression process at temperatures of 40°C, 45°C, and 50°C. These fluctuations usually relate to the irreversibility of the main compressor when it operates at high temperatures.

### 5.3 Effect of Main Compressor Inlet Temperature (MCIT)

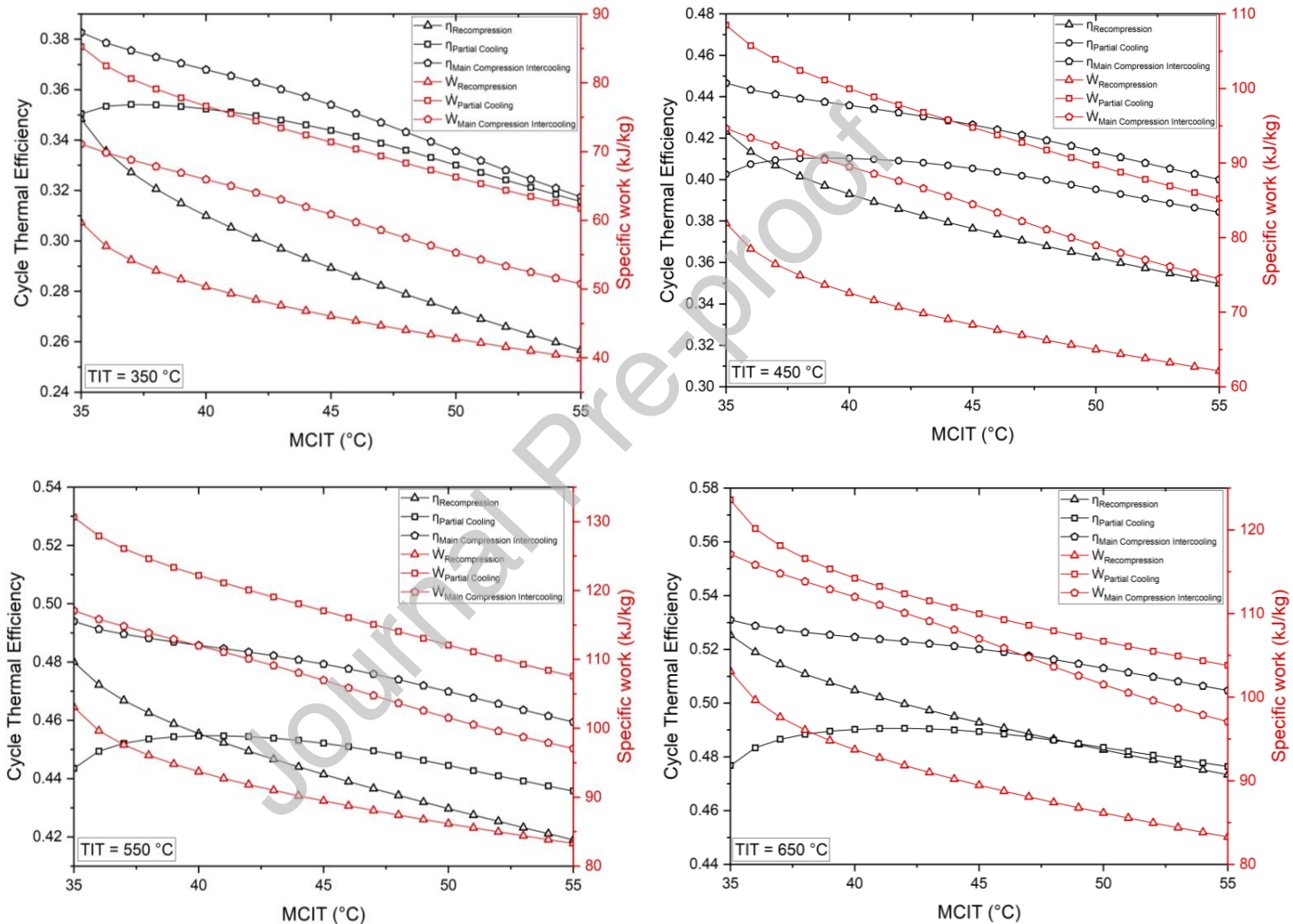


**Fig. 11.** Cycle thermal efficiency & specific work comparison for recompression, partial cooling & intercooling cycle with the variation of the MCIT at different turbine inlet temperature of 350°C, 450°C, 550°C and 650°C.

**Fig. 11** illustrates comparison of sCO<sub>2</sub> cycles thermal efficiency & specific work varying MCIT from 35°C to 55°C while keeping TIT fixed at certain temperatures to be investigated. In accordance with the Carnot efficiency, cycles that reject heat at a lower weighted average temperature will have higher efficiencies. Thus, reduction of MCIT results of increase  $\eta_{cycle}$  and as well as,  $W_{net}$ . It also demonstrates

that when temperature rises, work output and cycle efficiency decrease. Partial cooling cycle  $\eta_{cycle}$  increases at 40°C MCIT and then decreases due to the ideal cooling level that maximizes  $\eta_{cycle}$ . The precooler's failure to maintain ideal conditions causes a temperature drop when a threshold is reached. From the comparison, it is evident that main-compression intercooling sCO<sub>2</sub>BC provides better cycle thermal efficiency (53.2% at 650°C TIT), comparing to other two cycles.

#### 5.4 Impact of Pinch Temperature of Recuperator

The effect of the pinch temperature for the recuperator on the performance of sCO<sub>2</sub> Brayton cycles are also investigated. For recuperator  $T_{pinch}$  in the range of 7°C to 20°C, the cycles are optimized to obtain maximum cycle efficiency. **Fig. 12** shows the optimal split ratio and pinch temperature to produce the maximum  $\eta_{cycle}$ . As recuperator  $T_{pinch}$  increases, the ideal split ratio decreases from 0.65 to 0.632. Accordingly,  $\eta_{cycle}$  decreases steadily with increasing recuperator  $T_{pinch}$ . From an economic point of view, the main-compression intercooling cycle has an advantage over the recompression & partial cooling cycle, which has different splitting location of the working fluid.

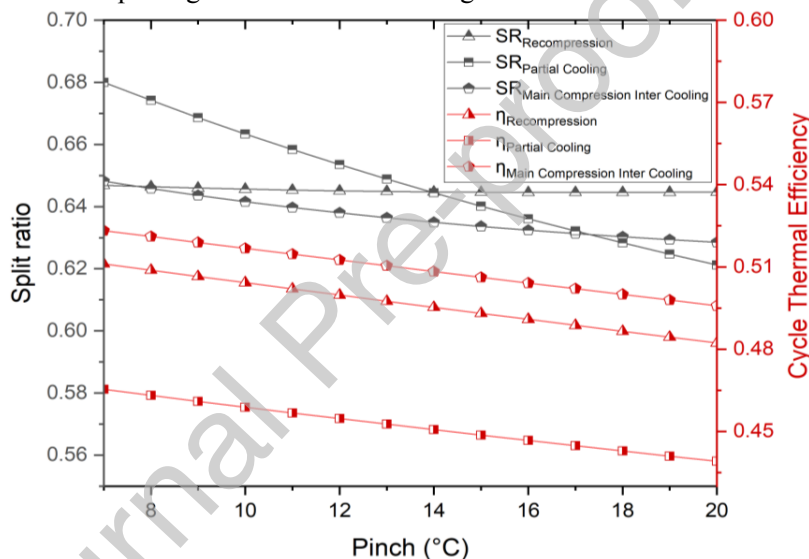


**Fig. 12.** Comparison of split ratio & cycle thermal efficiency with variation of recuperator pinch temperature.

#### 5.5 Impact of Isentropic Efficiency of Main Compressor

Although it was presumed that the compressor efficiency for all three cycles was 89%, the effect of main compressor efficiency on each cycle's performance should be investigated to make a fair comparison of the three cycles. **Fig. 13** shows the specific work, split ratio,  $\eta_{cycle}$  &  $\dot{m}$  of the recompression, partial cooling, and main-compression intercooling cycle for  $\eta_c$  ranging from 70% to 90% and a constant isentropic turbine efficiency ( $\eta_t = 90\%$ ). In the cases of the recompression and main-compression intercooling cycles, SR increases steadily with increasing isentropic efficiency of the main compressor. However, in the case of the partial cooling cycle, the split ratio has a decreasing curve. The main-compression intercooling cycle has a higher efficiency than the recompression and partial cooling cycles over a wide range of  $\eta_c$ , especially in the region of low  $\eta_c$ . Therefore, the main-compression intercooling cycle can achieve a higher efficiency at a lower main compressor efficiency.

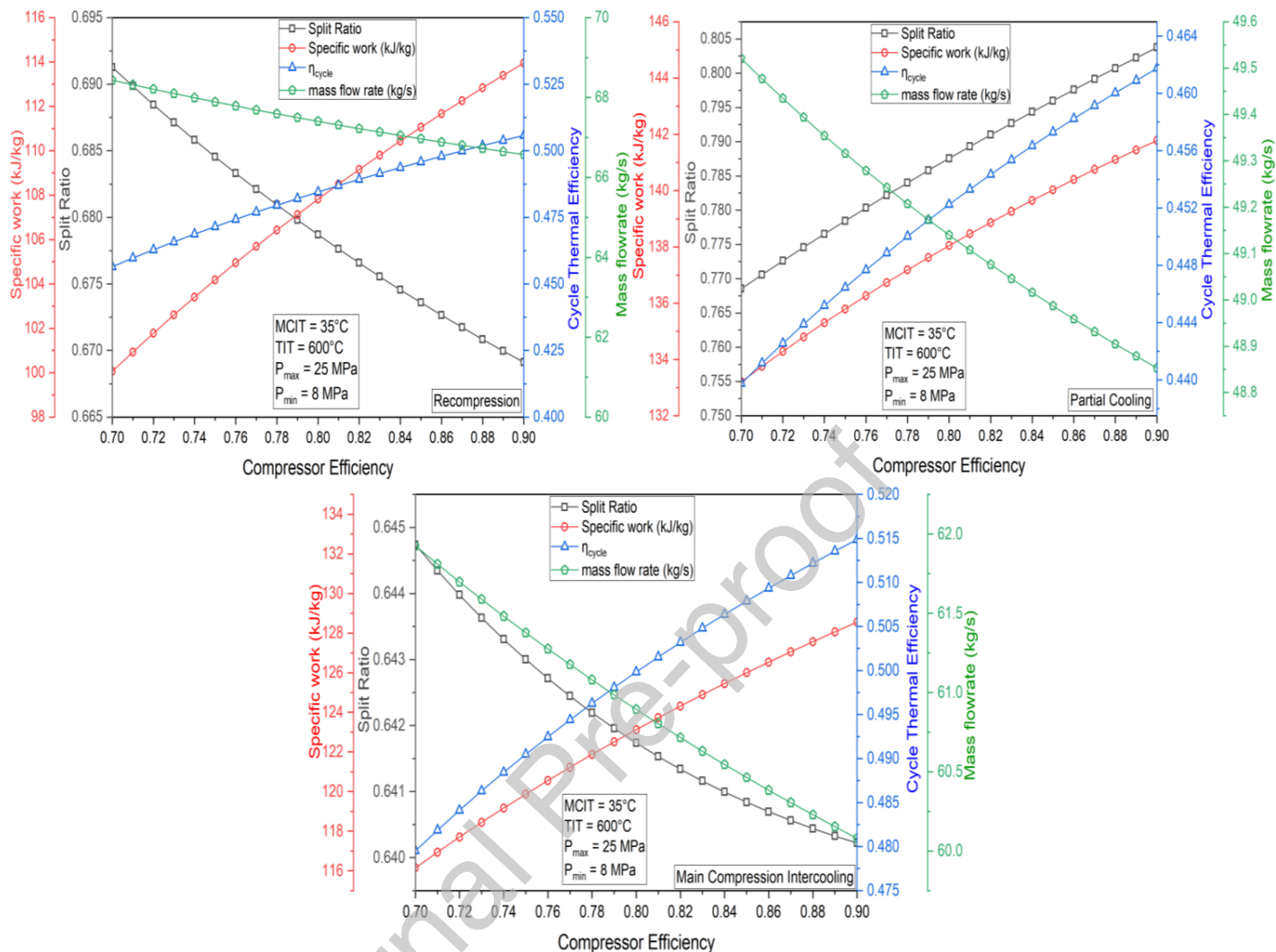


**Fig. 13.** Specific work, split ratio, cycle efficiency & mass flowrate of different sCO<sub>2</sub> cycle with the variation of compressor efficiency.

## 5.6 Exergy Destruction

**Fig. 14** illustrates Grassmann diagram representing each component's exergy destruction in an operational state of 25 MPa cycle  $P_{max}$ , 8 MPa cycle  $P_{min}$ , 600°C TIT and 34°C MCIT. The arrows represent the components and the width of the lines connecting the components was varied to visually represent the quantity of exergy flow. From the results, it can be seen that maximum exergy destruction of 5837.5953 kW (30.24%) occurs in the compressor, whereas insignificant exergy destruction is seen in the turbines.

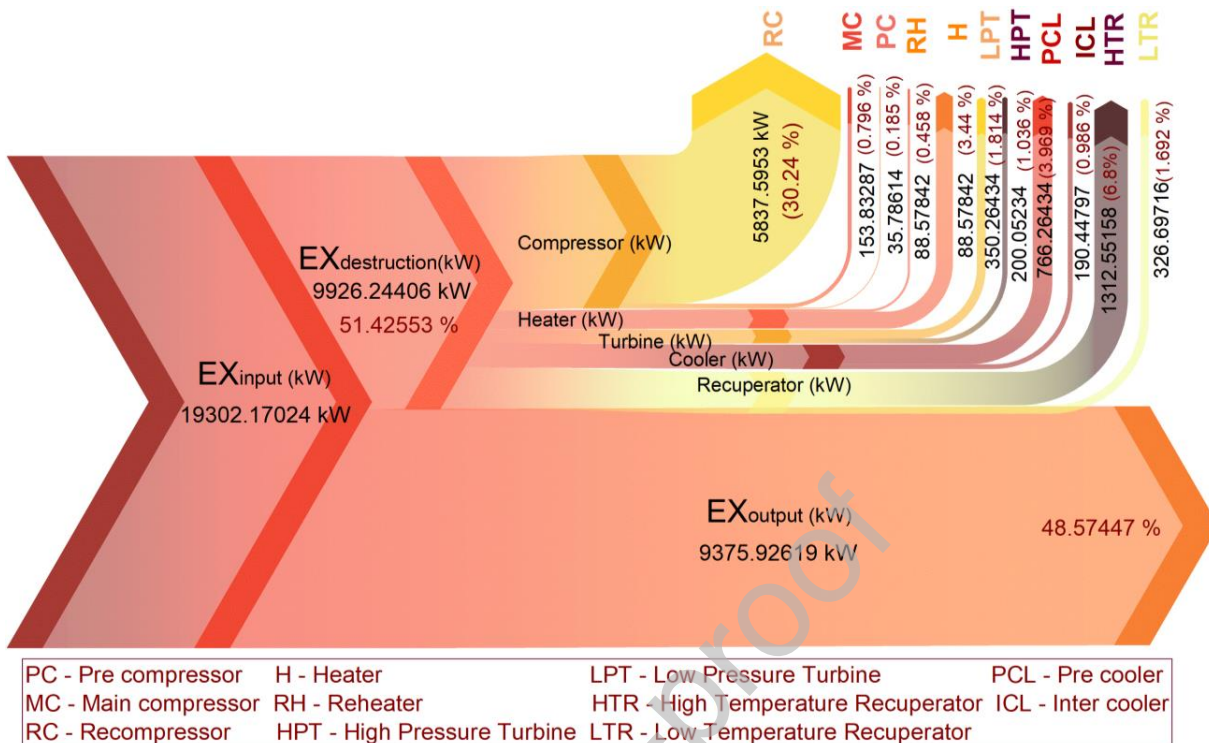


**Fig. 14.** Exergy destruction in different components in main compression intercooling sCO<sub>2</sub> cycle.

### 5.7 Effect of Air Temperature and DNI

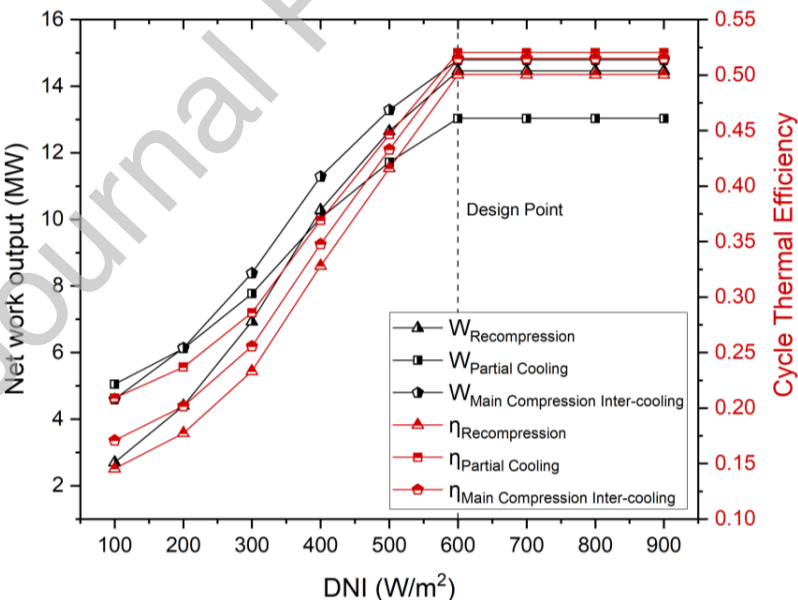


**Fig. 15.** Power output and cycle thermal efficiency at different DNI conditions.

Power output for recompression, partial cooling, and main-compression intercooling cycle at different DNI conditions is demonstrated in **Fig. 15**. Without TES arrangement, when the ambient temperature falls under the design point (MCIT=34°C & DNI=0.6 kW/m<sup>2</sup>), the CSP plant overcools. At critically lower air

temperatures, portion of heat from CSP loop is used in the cycle, to keep MCIT at 34°C throughout. When DNI rises above 600 W/m<sup>2</sup>, TIT is expected to increase as well resulting in more W<sub>net</sub>, however, this would make the turbines vulnerable due to metallurgical limitations. Hence, TIT is limited to 600°C regardless increase in DNI after the design point, providing constant thermal power output.

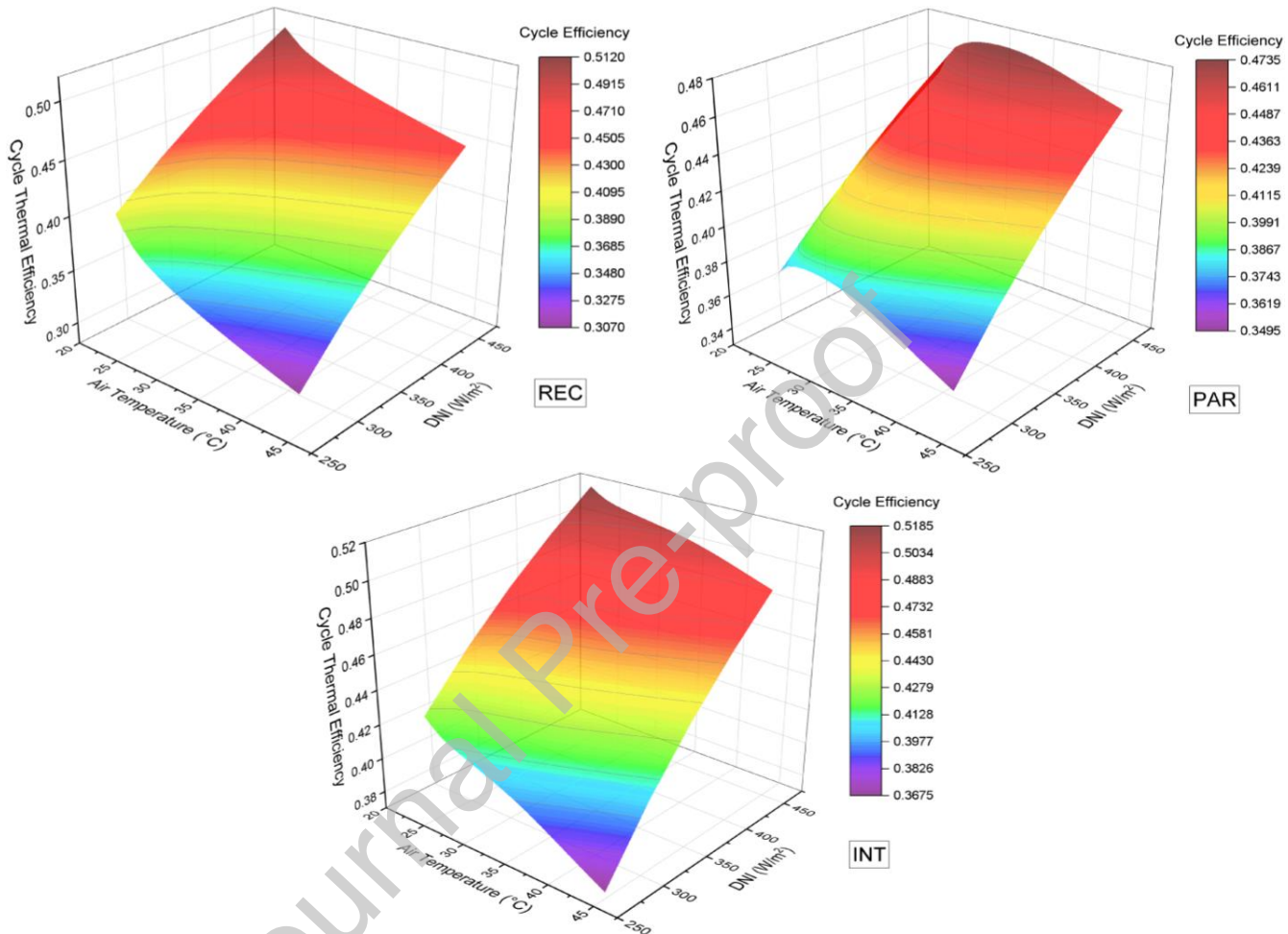


**Fig. 16.** The effect of air temperature and DNI on cycle thermal efficiency (a) Recompression sCO<sub>2</sub>BC, (b) Partial cooling sCO<sub>2</sub>BC, (c) Main compression intercooling sCO<sub>2</sub>BC.

**Fig. 16.** illustrates the trend between cycle thermal efficiency, air temperature, and DNI for three distinct functional cycles. The color gradients serve as visual representations of the varying levels of cycle efficiency. The efficiency of the cycle is negatively impacted by an increase in air temperature, with the optimal conditions being characterized by the lowest possible air temperature and the DNI values. The area exhibiting the lowest cycle efficiency for the INT cycle is observed when the air temperature falls between the range of 37 to 45°C, while the Direct Normal Irradiance (DNI) varies from 250 to 300 W/m<sup>2</sup>. However, for PAR cycle, an improvement in efficiency to 47.35% was initially observed when DNI rose and air temperature declined. Finally, these 3D plots indicate that the REC, PAR, and INT sCO<sub>2</sub> cycles achieve optimal cycle performance when operating under conditions characterized by low air temperatures and high DNI.

### 5.8 Dynamic Attributes of Plant Operation Under Various Climate Condition

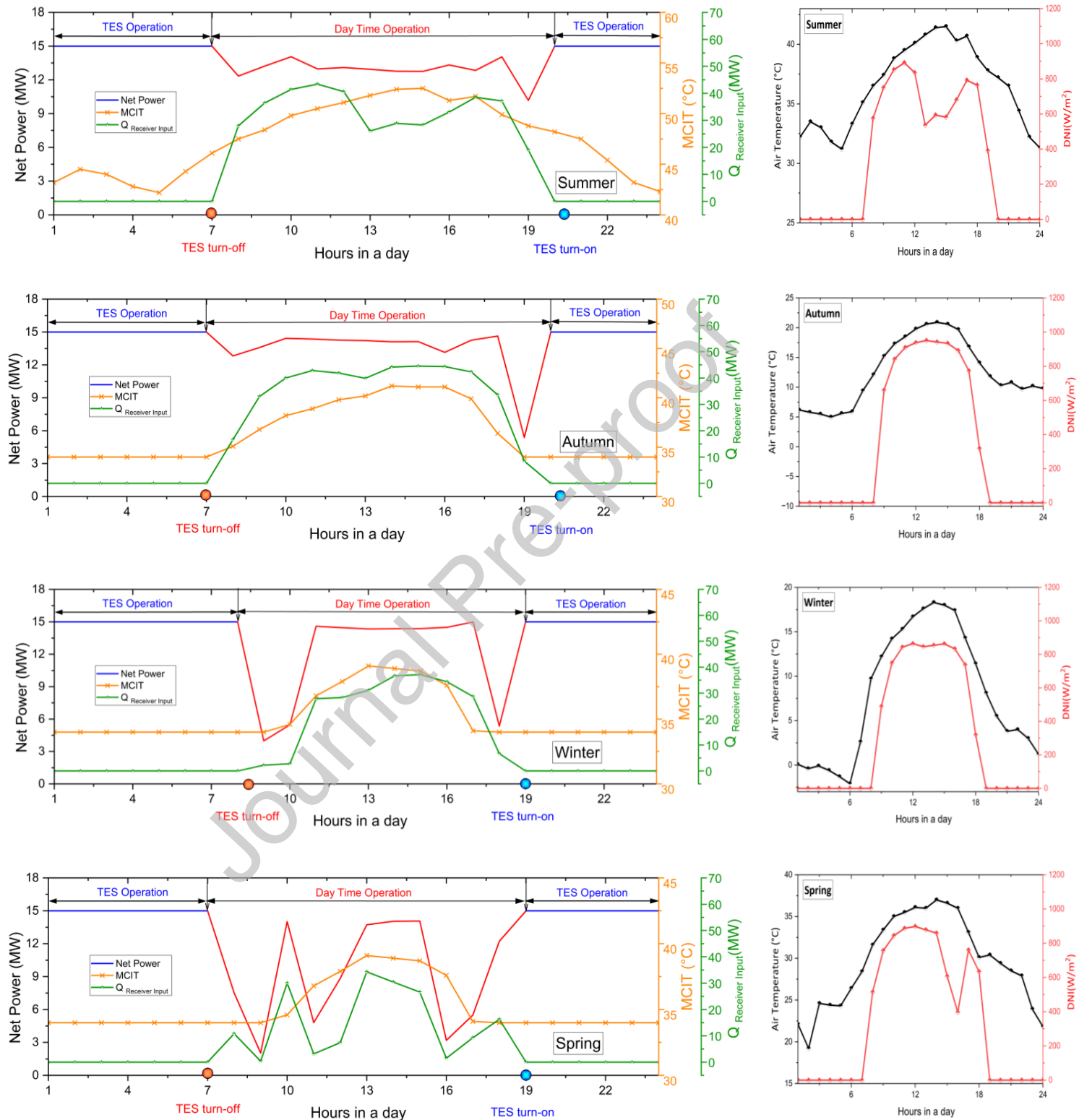


**Fig. 17.** Main compression intercooling  $s\text{CO}_2$  cycle hourly CSP plant performance for supplemented with TES at various seasonal climates.

**Fig. 17** shows hourly performance for sCO<sub>2</sub> cycle at varied seasonal climates, TES was incorporated. Since the temperature during the day consistently exceeds the design point, the core flow splitter alters the split ratio to increase energy output. Since the air temperature is consistently below the intended limit in autumn, the Natural Draft Dry Cooling Tower (NDDCT) flow divider is constantly in operation [37]. Similar performance is shown in the winter and spring, although because of the very low ambient temperature, the winter bypass percentage changes significantly. The primary flow divider is essentially constant throughout the autumn, winter, and spring. TES is switched off at 7:00 a.m., and the cycle is thereafter powered by solar energy. Power output is limited by variations in the temperature of the turbine caused by variations in solar energy. Additionally, the quantity of solar salt that flows between the power block and the central receiver is constantly regulated by changes in DNI. Since solar energy is irregular a key characteristic that constantly changes is the bulk flow of molten salt. When there is no solar energy available in the evening around 19:00, using the molten salt in the heated reservoir TES switches to discharge mode. The CSP plant built for DP (15MW) demonstrates increased steadiness in power output while running under TES as almost constant heat is supplied to the turbine. The performance fluctuates greatly on other days throughout each season; therefore, the graph above does not really assess the best seasonal environment for maximizing power output. The steam cycle's thermal efficiency increases as MCIT decreases. For sCO<sub>2</sub> power cycles, however, this is not true since lowering the operating fluid's temperature below the pseudocritical point can seriously damage the compressor's ability to operate properly. Furthermore, according to earlier studies, a cold climate requires a higher thermal input for the sCO<sub>2</sub> power cycle. A broader solar field is thus required for CSP applications to run the power cycle when the air is cooler and collect more thermal energy from the central receiver. In this study, it is avoided that the sCO<sub>2</sub> power cycle's subcritical operation and NDDCT design. Operation instability of the compressor results from the sCO<sub>2</sub> power cycle operating in subcritical state.

## 6. Multi-objective Optimization

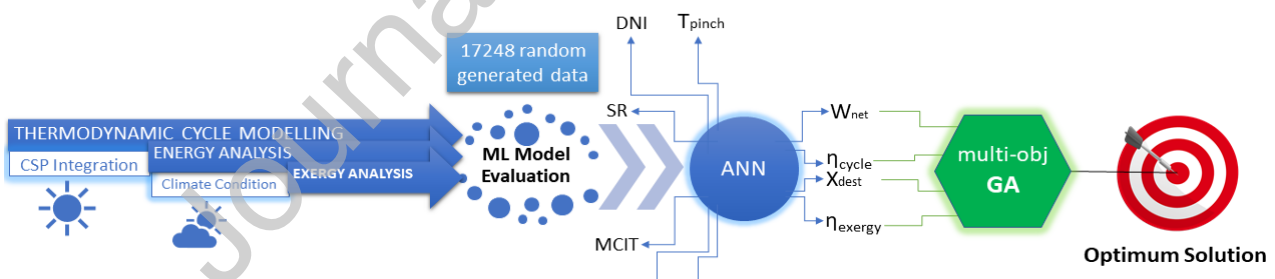


**Fig. 18:** Optimization methodology framework.

Main-compression intercooling sCO<sub>2</sub>BC is chosen for optimization as this system outperforms recompression & partial cooling cycle in terms of thermal performance at different operating conditions. **Fig. 18.** shows the outline of the optimization methodology used in this study. Once the data required has been calculated, to find the sensitivity of the input parameters, the generated values are initially analyzed with a sensitivity analysis. Based on computing requirements and ML model prediction accuracy, the most optimal model is chosen. The use of artificial neural networks (ANNs) into the optimization of advanced sCO<sub>2</sub> power cycles presents numerous benefits in comparison to conventional thermodynamic models. ANNs have been shown to enhance accuracy through their ability to capture intricate, non-linear

interactions. Additionally, ANNs enable adaptability in accommodating diverse situations and complexities within a given system. They have exceptional proficiency in managing complex systems, enabling quick adjustments in response to changing circumstances, leveraging data-driven analysis to inform decision-making, and expediting the process of software development. ANNs have the potential to significantly improve energy efficiency, rendering them highly valuable in various domains, including power generation. Nevertheless, it is imperative to utilize these tools along with thermodynamic models in order to optimally utilize their capabilities while effectively addressing their limits. To optimize design parameters, multi-objective GA is integrated with the best machine learning model. MATLAB software is used for setting up neural network & GA- gamultiobj was set as solver for multi-obj optimization. The following subsections provide insights regarding the adopted framework for this study.

### 6.1 Sensitivity Analysis

Using the Weighted Least Square (WLS) technique, a sensitivity analysis has been conducted. A heat map, **Fig. 19**, depicts sensitivity and correlation between the input and output parameters. A greater number indicates that the column's parameters are more sensitive to changes in the row's values[2]. Conversely, the trends of the output numbers are caused by the input parameters are shown by positive and negative signs as being direct or inverse. The output parameter, net work is sensitive to all input factor where, DNI is the most sensitive input parameter.

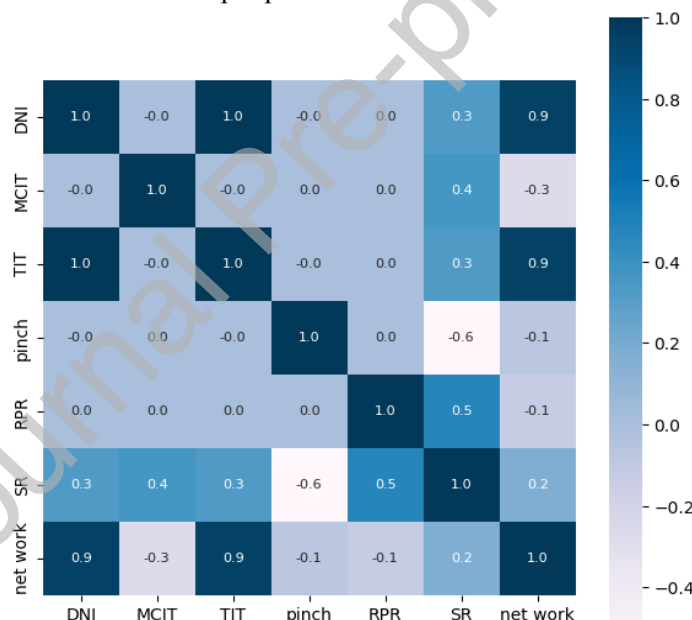


**Fig. 19:** Heat map showing the sensitivity of cycle parameters to the variation in output variables.

### 6.2 Methodology of ML based Algorithms

In the current work, six machine learning algorithms, specifically XGBoost, Random forest, LightGBM, AdaBoost, KNN, and ANN are used to train the data. On the basis of prediction accuracy, the best model is chosen for next stage of optimization. The following subsections present details about the theoretical framework used in the study.

### 6.2.1 XGBoost Algorithm

The supervised learning algorithm XGBoost, accurately predicts a target variable by combining the values of simpler variables. It implements regression trees as weak learners and minimizes the objective function by means of a convex loss function and penalty clause. The training procedure is iterative, with the addition of new trees for forecasting residues and errors and the execution of gradient boosting to minimize loss. Instead of selecting the best model based on the data, XGBoost parallelizes the dataset's boosting by training hundreds of models on diverse subsets[38].

$$F_n(X) = F_{n-1}(X) + \alpha_{n-1} g_j(X, q_{n-1}) \quad (07)$$

Here,

$\alpha_j, q_j$  = regularization parameters and residual computing  $j^{\text{th}}$  tree.

$g_j$  = function used to train the prediction of residuals

For computing  $\alpha_j$  we first compute the residual then use this function

$$\arg \min(\alpha) = \sum_{j=1}^n L(Y_j, F_{j-1}(X_j) + \alpha g_j(X_j, q_{j-1}))$$

where  $L(Y, F(X))$  differentiable loss function

### 6.2.2 Random Forest Algorithm

The RF approach, which combines multiple independent decision trees to precisely anticipate new input data, is a key part of machine learning's supervised learning strategy. Ensemble learning solves classification and regression problems. Using each tree's projections and predictions, Optuna hyperparameter tweaking minimizes overfitting and maintains accuracy [39]. Least squares create the decision tree,  $x(n)$  was separated into  $R1$  and  $R2$  after choosing the separation point (sp). Calculating the minimal output  $y$  value by calculating  $c1$  and  $c2$ . This means that  $(n)$  is this ap's optimal separation point from  $x$ .

$$\min_{sp} [\min_{c1} \sum_{xi \in R1} (yi - c1)^2 + \min_{c2} \sum_{xi \in R2} (yi - c2)^2] \quad (08)$$

The value of the output will be calculated for each node. Here,  $R1$  is shown as an example. The output value of this node will be:

$$C_{0=\frac{1}{N1}} \sum_{xi \in R1} yi \quad (09)$$

### 6.2.3 LightGBM Algorithm

LightGBM is a data structure that applies the GBDT algorithm, combines weak learners, and sets up a regression tree. It enhances accuracy and efficiency by splitting continuous eigenvalues into k-intervals and avoiding overfitting through regularization. Also, the objective function is efficiently approximated using Newton's approach. [40]. The objective function can be expressed as

$$Obj^{(n)} \cong \sum_{n=1}^m \left[ g_n f_n(x_n) + \frac{1}{2} h_n f_n^2(x_n) \right] + \sum_k \Omega(f_k) \quad (10)$$

Where,  $g_n$  &  $h_n$  denotes two loss functions: a first-order loss function and a second-order loss function, respectively.

$$g_n = \partial_{F_{n-1}(x_i)} \Psi(y_n, F_{n-1}(x_i)) \quad (11)$$

$$h_n = \partial_{F_{n-1}(x_i)}^2 \psi(y_n, F_{n-1}(x_i)) \quad (12)$$

The algorithm implements a leaf-wise generation strategy to minimize training data and eliminate overfitting. By integrating high-dimensional data features in a sparse feature space, the EFB algorithm of LightGBM prevents redundant features[41].

#### 6.2.4 AdaBoost

AdaBoost's classifier or regression functions use an array of stumps that are iteratively trained using feature data ( $x$ ) and target data ( $y$ ). The algorithm's overall predictions are obtained immediately after training using a weighted average of the predictions from the stumps. Weak classifiers  $\{\varphi_\mu(x) : \mu = 1, \dots, M\}$ . Known data  $X = \{(x_i, y_i) : i = 1, \dots, N\}$  where  $y_i \in \{\pm 1\}$ . here  $\lambda_\mu$  weights that must be developed. AdaBoost's final regression solution is asymptotic. This is partially accurate due to technological issues and data growth. AdaBoost Regression improves results but requires additional computations. Furthermore, it necessitates the execution of the sparsity requirement that the diversity of  $\lambda$ 's be zero.[42]

$$P(y | x) = \frac{e^{y \sum_\mu \lambda_\mu \phi_\mu(x)}}{e^{\sum_\mu \lambda_\mu \phi_\mu(x)} + e^{-\sum_\mu \lambda_\mu \phi_\mu(x)}} \quad (13)$$

#### 6.2.5 K Nearest Neighbor (KNN) Algorithm

KNN is a popular regression technique that calculates distances between neighbors using weighting techniques. It provides more accuracy but is time-consuming. However, it necessitates adaptive neighbors and weighting to accommodate dataset properties, and traditional KNN may not be accurate due to dataset density variations.[43]. Let  $\{N_i^j\}^k$  represent the target values of an instance's  $k$  nearest neighbors. After that, the conventional KNN prediction  $Y_i$  for the  $i$ -th instance is calculated as shown below:

$$Y_i = \frac{1}{k} \sum_{j=1}^k N_i^j \quad (14)$$

#### 6.2.6 Artificial Neural Network (ANN)

The configuration of the ANN algorithm is shown in **Table 15**. A feedforward net neural network integrated into MATLAB was utilized, and the inputs were divided at random (dividerand), as shown **Fig. 20**. Ideally, the number of neurons for the analysis should be set to 10. The feedforward neural network is a versatile tool that can be employed for various types of input-output mappings. The performance metric employed in this study is the Mean Squared Error (MSE), whereas the training method utilized is Bayesian regularization (trainbr). Although the trainbr approach normally takes longer, it may provide a high degree of generalization for difficult, constrained, or noisy datasets and adaptive weight minimization determines when training ends.

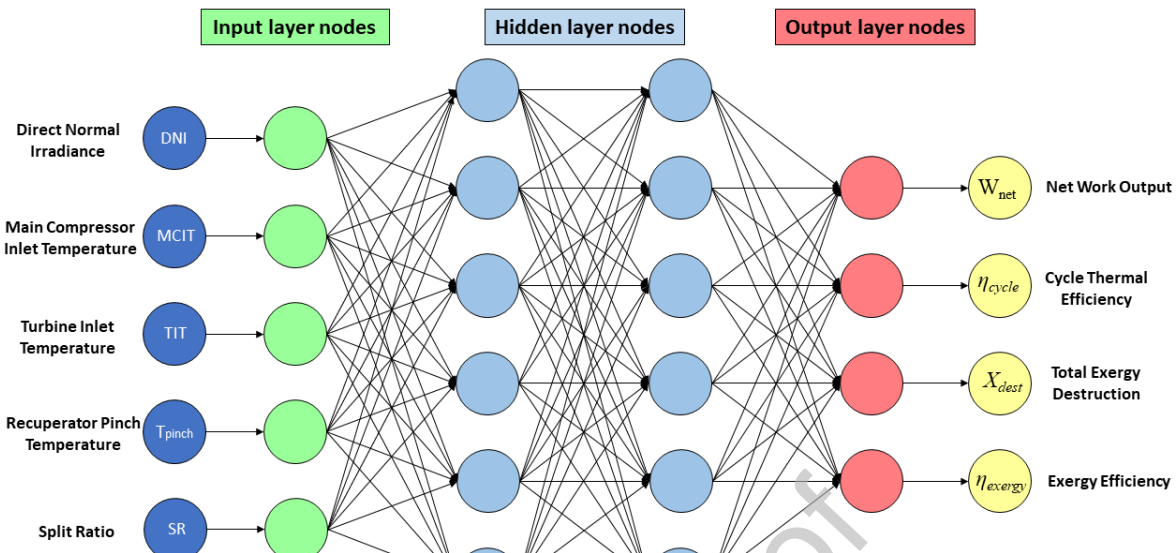


**Fig. 20.** Artificial neural network.

**Table 15:** ANN algorithm setup.

Data Division	Training	Performance	Calculations
dividerand	trainbr	MSE	MEX

### 6.3 Optimization Methodology

A genetic algorithm is a population-based feature selection method that chooses from a variety of solutions instead of limiting to just a single. The genetic algorithm's fundamental objective is to find the optimal solution from the population in the shortest amount of time [44]. MATLAB in-built neural network tool is used to train the model and generate the function that is utilized in multi-obj GA to carry out the optimization process using the input parameters included in **Table 16**. The GA evaluates the population using the objective function. **Table 17** outlines the range of input parameters (LB-lower bounds & UB-upper bounds) for multi-objective optimization for REC, PAR & INT sCO<sub>2</sub>BC.

**Table 16:** GA problem setup parameter options.

Parameters	Options	Values
Population	Type: Double vector	Population size: 200
Selection	Function: Tournament	Size: 2
Mutation	Constraint dependent	-
Migration	Direction: Forward	Fraction: 0.2, Interval: 20
Multiobjective problem settings	Function: @distancecrowding	Fraction: 0.35
Stopping criteria	Function tolerance	Specify: 0
Plot functions	Pareto front	-

**Table 17:** Range of input parameters for optimization.

Cycle	REC	PAR	INT			
Parameters	LB	UB	LB	UB	LB	UB
DNI (kW/m <sup>2</sup> )	0.27187	0.65312	0.271875	0.653125	0.27187	0.65312

MCIT(°C)	34	55	34	55	34	55
TIT (°C)	400	700	400	700	400	700
T <sub>pinch</sub> (K)	5	20	5	20	5	20
RPR	-	-	0.3	0.9	0.3	0.9
SR (x)	0.6445	0.7968	0.23	0.98	0.5566	0.8

#### 6.4 TOPSIS Method

In multi-criteria decision-making, ranking reversal is a problem when a selection method or alternative set shifts. This issue is fundamental to decision-making and multi-criteria decision-making discussions. According to Alirahmi et al.[45] assuming K decision-makers are evaluating  $m$  decisions based on  $n$  criteria and weights combined using the arithmetic mean or other methods, i.e., the traditional TOPSIS method's appropriate approach, the sum of the ratings and weights is then utilized to generate the decision ( $D$ ) and weight ( $W$ ) matrix depicted below [46]:

$$D = \begin{bmatrix} x_{11} & x_{12} & \cdots & x_{1n} \\ x_{21} & x_{22} & \cdots & x_{2n} \\ \vdots & \vdots & \ddots & \vdots \\ x_{m1} & x_{m2} & \cdots & x_{mn} \end{bmatrix}$$

$$W = [w_1 \quad w_2 \quad \cdots \quad w_n]$$

Subjected to

$$x_{ij} = \text{aggregate rating of } i^{\text{th}} \text{ alternative for } j^{\text{th}} \text{ criterion}$$

$$w_j = \text{the weight for } j^{\text{th}} \text{ criterion}$$

Vector or linear normalization is used to scale up diverse criteria to a similar level. Decision matrix ( $R$ ) that has been normalized by[46]:

$$R = \begin{bmatrix} r_{11} & r_{12} & \cdots & r_{1n} \\ r_{21} & r_{22} & \cdots & r_{2n} \\ \vdots & \vdots & \ddots & \vdots \\ r_{m1} & r_{m2} & \cdots & r_{mn} \end{bmatrix}$$

Subjected to

$$r_{ij} = \text{normalized rating of } i^{\text{th}} \text{ alternative for } j^{\text{th}} \text{ criterion}$$

Chen el al.[47] suggested a linear method to construct a decision matrix, which illustrates how the alternatives perform against each criterion. To maintain impartiality, raw data is normalized into dimensionless values. To weight decision-making aspects, many weighing methods are investigated.

$$i_{opt} \in \max \left\{ \frac{ED_i^+}{ED_i^+ + ED_i^-} \right\} \quad (15)$$

$$B_{ij} = F_{ij} / \sqrt{\sum_{i=1}^m F_{ij}^2}, G_{ij} = w_j^{TOPSIS} \cdot B_{ij} \quad (16)$$

$$ED_i^- = \sqrt{\sum_{j=1}^m (G_{ij} - G_j^{\text{negative}})^2} \quad (17)$$

In Equation (16),  $w_j^{\text{TOPSIS}}$  is the weight of the  $j$ -th optimization objective,  $G_j^{\text{negative}}$  is the value of the  $j^{\text{th}}$  target with an NIP (negative ideal point) after normalization, and Distance  $i$  is the Euclidean distance between the  $i^{\text{th}}$  feasible option and (NIP) [48]. For a simple computation,  $w_j^{\text{TOPSIS}} = 1$  is utilized in this study.

The ideal ( $P^+$ ) & negative-ideal ( $P^-$ ) strategies are determined as Equations (18) and (19), respectively[49]:

$$P^+ = \{v_1^+, \dots, v_n^+\} = \left\{ \left( \max_j v_{ij} \mid i \in R' \right), \left( \min_j v_{ij} \mid i \in R^- \right) \right\} \quad (18)$$

$$P^- = \{v_1^-, \dots, v_n^-\} = \left\{ \left( \min_j v_{ij} \mid i \in R' \right), \left( \max_j v_{ij} \mid i \in R^- \right) \right\} \quad (19)$$

## 6.5 ML Model Accuracy Check & Error Evaluation

Machine learning models are evaluated by comparing their performance using metrics such as  $R^2$  and RMSE values. For dataset sizes greater than 3500 samples, a significant drop in the RMSE values for the three objective functions may be seen[50]. **Fig. 21**, **Fig. 22** and **Fig. 23** illustrates prediction result curve for cycle thermal efficiency, power output, exergetic efficiency and comparison between ML algorithms  $R^2$  score for both train & test datasets, respectively. Machine learning issues encompass the phenomena of overfitting and underfitting. A model exhibit overfitting on the training data, as it tends to incorporate irrelevant or random fluctuations, hence reducing its ability to generalize to unknown data. The occurrence of underfitting emerged prominently in the case of K-nearest neighbors (KNN), indicating that this particular model is extremely simplistic and lacks the ability to effectively capture crucial patterns present in the dataset. ANN shows best prediction score (Test = 0.99941 & test = 0.99855) compared to other models: ANN > XGBoost > RF> LightGBM > AdaBoost > Ridge > KNN > ElasticNet > Lasso.

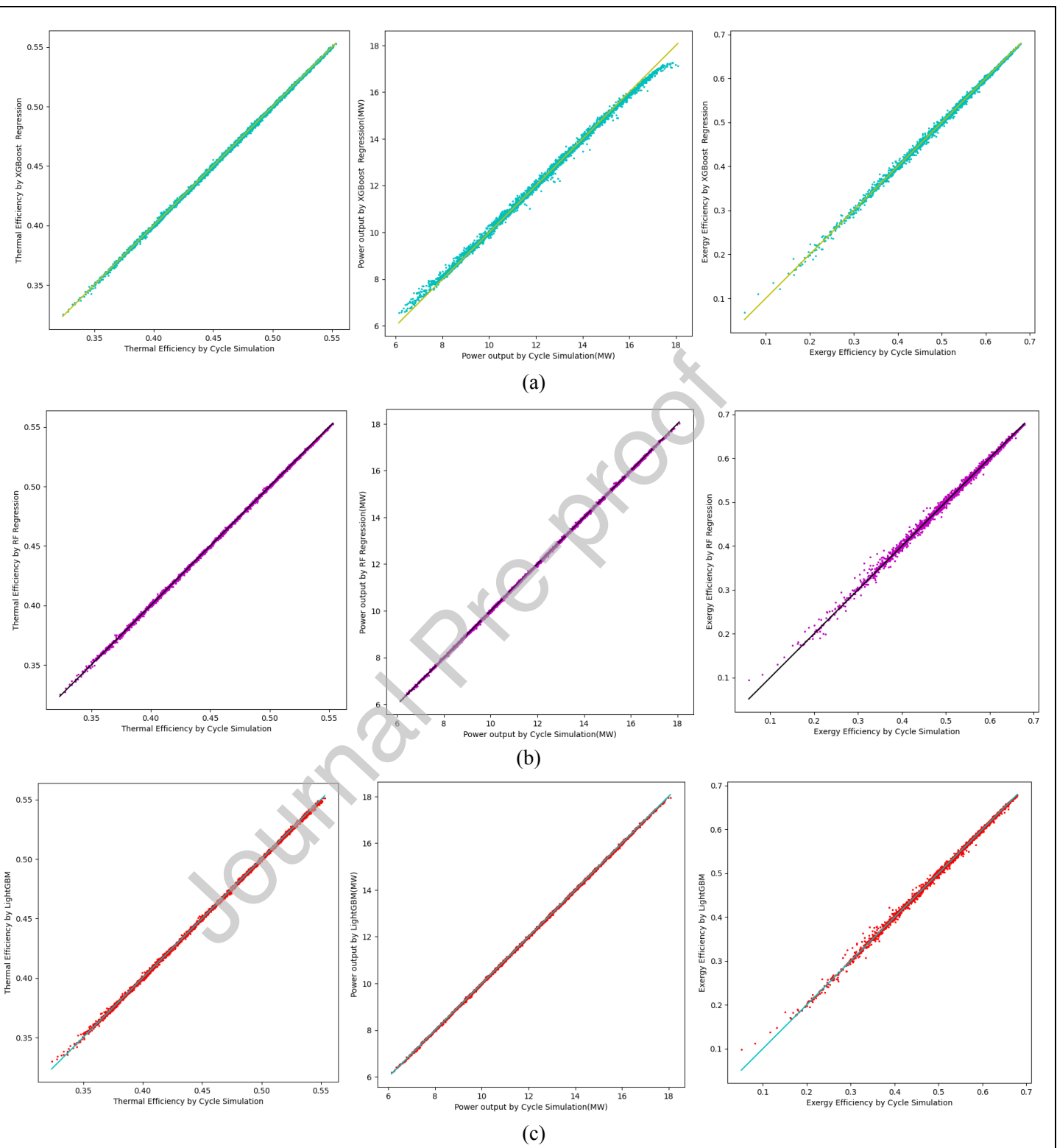


**Fig. 21.** Prediction result for thermal efficiency(left), power output(mid) and exergy(right) efficiency of main compression intercooling cycle for (a)XGBoost, (b)RF, (c)LightGBM.

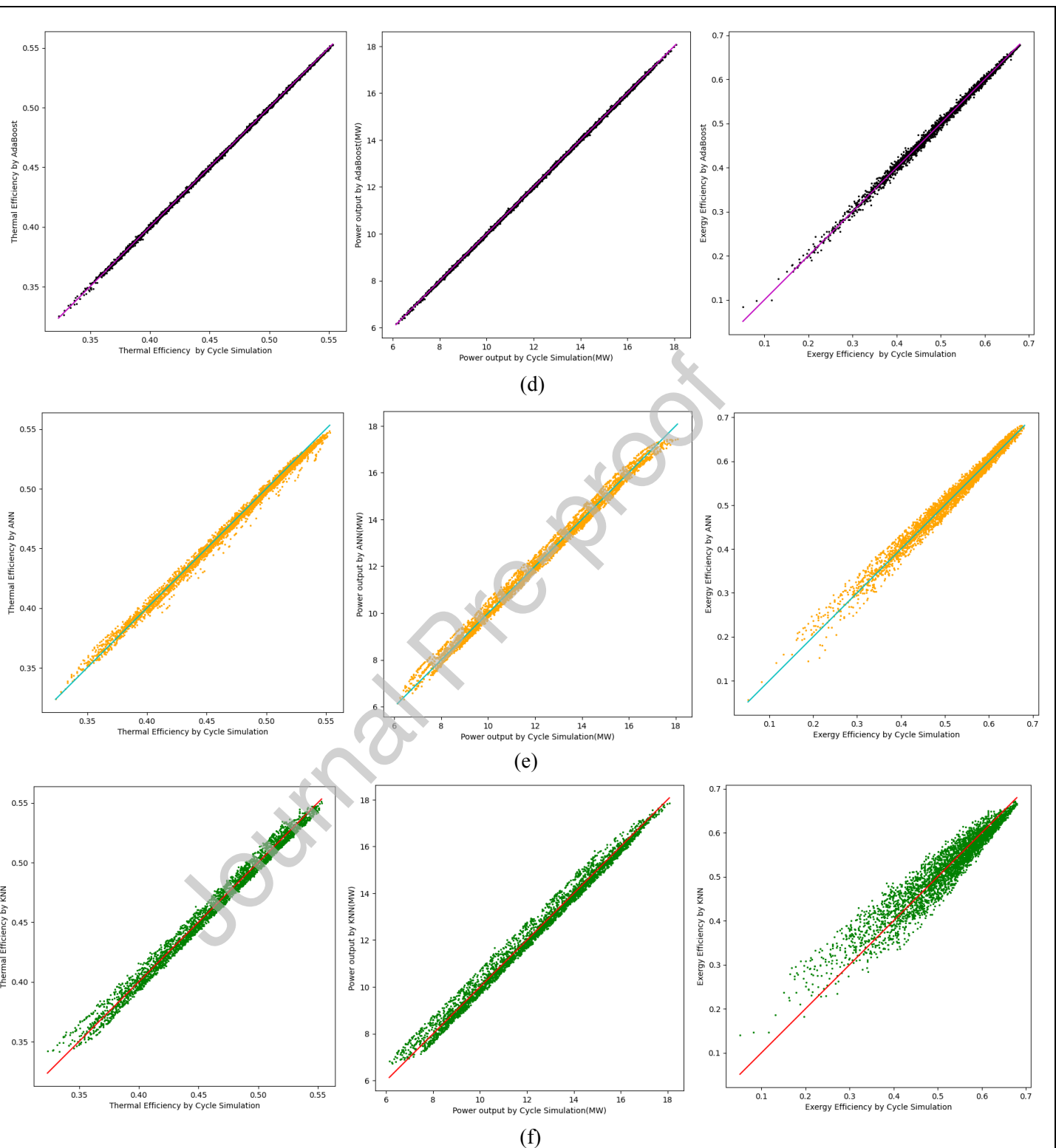


**Fig. 22.** Prediction result for thermal efficiency(left), power output(mid) and exergy(right) efficiency of main compression intercooling cycle for (d)AdaBoost, (e)ANN, (f)KNN.

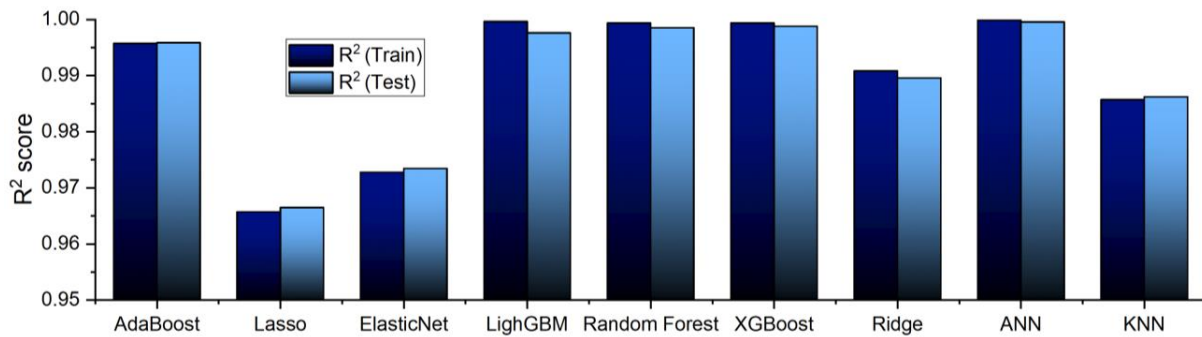


**Fig. 23.** Prediction score (test & train) comparison of different machine learning models.

## 6.6 Optimization Result

The comprehensive list of the optimal design conditions generating the Pareto front for main-compression intercooling cycle (**Fig. 24**) is included in **Table 17**. Pareto front shows a reasonable compromise between Objective-1 ( $W_{net}$ ) and Objective-2 ( $X_{dest}$ ) and displays the greatest ranges of the net power output. TOPSIS decision making tool is utilized for choosing optimized configurations. **Table 18** shows the conditions for (A) maximum exergy destruction, (B) optimal point & (C) maximum work output, obtained from pareto front diagram.

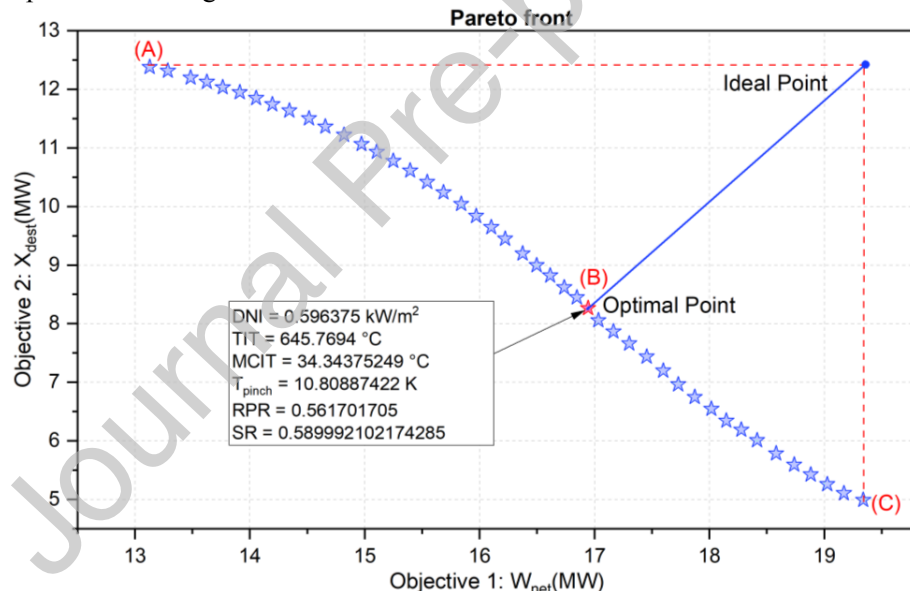


**Fig. 24.** Pareto front calculated by coupling ANN with a multi-objective genetic algorithm for INT sCO<sub>2</sub>BC.

**Table 18:** Pareto front input & output variables for optimal & maximum points.

Points	Condition	DNI, kW/m <sup>2</sup>	MCIT, °C	TIT, °C	T <sub>pinch</sub> , K	RPR	SR	W <sub>net</sub> , MW	X <sub>dest</sub> , MW
(A)	Max. Exergy Destruction	0.565852	34.19028	629.6794	19.7702	0.883539	0.646379	13.12637	12.38015
(B)	Optimal	0.596375	34.34375	645.7694	10.80887	0.561702	0.589992	16.985	8.167
(C)	Max. Work Output	0.653125	34.12277	660.998	9.078243	0.49408	0.566457	19.33925	4.99355

**Table 19:** Values of the input layer functions corresponding to the optimal solution obtained using TOPSIS.

Optimization variables	Unit	Recompression	Partial cooling	Main compression intercooling
Direct normal irradiance, $DNI$	$kW/m^2$	0.608273	0.621001	0.596375
MCIT	$^{\circ}C$	40.328	34.047	34.344
TIT	$^{\circ}C$	662.414	687.4	645.769
Pinch temperature, $T_{pinch}$	K	11.12	12.19	10.81
Ratio of pressure ratios, $RPR$	-	-	0.825	0.562
Split ratio, $SR$	-	0.6531	0.7106	0.5899
Net power output, $W_{net}$	MW	15.561	16.902	16.985
Thermal efficiency, $\eta_{cycle}$	%	53.028	46.833	54.708
Exergy destruction, $X_{dest}$	MW	4.697	7.961	8.167
Exergetic efficiency, $\eta_{exergy}$	%	77.896	67.533	63.619

**Table 19** highlights the optimized parameters ( $DNI$ ,  $MCIT$ ,  $TIT$ ,  $T_{pinch}$ ,  $RPR$ ,  $SR$ ) obtained from this study using different tools for best cycle performance ( $W_{net}$ ,  $\eta_{cycle}$ ,  $X_{dest}$ ,  $\eta_{exergy}$ ) for Recompression, Partial cooling & Main compression intercooling sCO<sub>2</sub> cycle. The thermal efficiency of the optimized concentrated solar power (CSP) integrated main compression intercooling system exhibits an enhancement from 50.845% to 54.708%, resulting in a substantial increase of 7.59%. This improvement facilitates the generation of a greater amount of energy. Simultaneously, a reduction in the turbine inlet temperature from 675 K to 645.769 K is observed, indicating a better utilization of the heat source, while achieving a net power output of 16.985 MW. Furthermore, the optimized power cycle exhibits enhanced efficiency, as indicated by a notable 15.67% increase in exergy efficiency under the specified conditions. In regard to the recompression and partial cooling cycle, the optimized net power production is determined to be 15.561 MW and 16.902 MW, respectively. The aforementioned data provide evidence that the utilization of the optimization approach has shown to be effective in determining the ideal parametric values of the power plant, resulting in enhanced thermodynamic performance. However, it is worth noting that a slight variation in input data may yield different optimized values.

## Conclusion

In this study, an optimization method is proposed based on GA for predicting the physical state and thermodynamic performance of sCO<sub>2</sub> power cycles from their design parameters. A comprehensive framework for numerical analysis and optimization is stated, considering CSP as heat source. To improve continuous power production when there is no solar insolation, the power block is equipped with TES. In addition, performance evaluations are made between three cycles in this work for solar power towers at the same solar subsystem (heliostats + receiver) conditions. The process of data collecting involves conducting calculations on recompression, partial cooling, and main compression intercooling in a sCO<sub>2</sub> cycle. These calculations are performed to assess the effectiveness of machine learning models. A total of 17,248 cases were collected by altering the important parameters. Out of these cases, 70% were allocated for use in training. The determination of the optimum set of the design parameters is achieved through the integration of a trained artificial neural network (ANN) with a multi-objective genetic algorithm. According to the preceding work, the following are the conclusions:

- Thermodynamic analysis reveals that under specific operating conditions, main compression intercooling sCO<sub>2</sub>BC thermodynamic performance is better than the recompression and partial cooling cycle.
- Exergy analysis reveals that that component with the greatest exergy destruction is the compressor (5837.5953 kW), making the compressor a crucial component of the sCO<sub>2</sub> cycle and optimization procedure.
- The impact of TES at night and the resulting system dynamic response is investigated as well. Heat rejection in the tower, tower outlet temperature, and net power generation are evaluated year-round under a variety of solar insolation and ambient temperature.
- ANN outperformed Random Forest, XGBoost, LightGBM, AdaBoost, and KNN in predicting  $\eta_{cycle}$  and  $W_{net}$ . ANN predicted 99% thermal efficiency and net power production data with 98% accuracy. When training sizes for complex systems are compared, the model still performs well when training sizes are reduced (from 70% to 50%), demonstrating that the model may lower the expense of sampling complicated systems.
- Thermodynamic optimization has shown that the suggested system is capable of achieving the best power production and thermal efficiency, 16.985 MW and 54.708%, respectively, at 34.344°C of MCIT.

The sCO<sub>2</sub> cycles presented in this paper can be investigated for use in waste heat recovery systems and nuclear reactors. Novel cycle configuration and operating conditions-independent models can be developed by global sensitivity analysis and optimization. Subsequently, the model needs previous sampling by modelling calculation in the design space, and research including active learning and transfer learning could reduce data required. These investigations would improve the efficiency and generalizability of ANN-GA based models for digital thermodynamic systems.

## REFERENCES

- [1] M.W. Faruque, Y. Khan, M.H. Nabil, M.M. Ehsan, Parametric analysis and optimization of a novel cascade compression-absorption refrigeration system integrated with a flash tank and a reheat, *Results in Engineering*. 17 (2023). <https://doi.org/10.1016/j.rineng.2023.101008>.
- [2] M. Saeed, A.S. Berrouk, Y.F. Al Wahedi, M.P. Singh, I.A. Dagga, I. Afgan, Performance enhancement of a C-shaped printed circuit heat exchanger in supercritical CO<sub>2</sub>Brayton cycle: A machine learning-based optimization study, *Case Studies in Thermal Engineering*. 38 (2022). <https://doi.org/10.1016/j.csite.2022.102276>.
- [3] Y. Khan, R.S. Mishra, Performance analysis of solar driven combined recompression main compressor intercooling supercritical CO<sub>2</sub> cycle and organic Rankine cycle using low GWP fluids, *Energy and Built Environment*. 3 (2022) 496–507. <https://doi.org/10.1016/j.enbenv.2021.05.004>.
- [4] M.M. Ehsan, S. Duniam, Z. Guan, H. Gurgenci, A. Klimenko, Seasonal variation on the performance of the dry cooled supercritical CO<sub>2</sub> recompression cycle, *Energy Convers Manag.* 197 (2019) 111865. <https://doi.org/https://doi.org/10.1016/j.enconman.2019.111865>.
- [5] S.M. Besarati, D. Yogi Goswami, Analysis of Advanced Supercritical Carbon Dioxide Power Cycles With a Bottoming Cycle for Concentrating Solar Power Applications, *J Sol Energy Eng.* 136 (2013). <https://doi.org/10.1115/1.4025700>.
- [6] M. Persichilli, A. Kacludis, E. Zdankiewicz, T. Held, Supercritical CO<sub>2</sub> Power Cycle Developments and Commercialization: Why sCO<sub>2</sub> can Displace Steam Steam, n.d. [www.echogen.com](http://www.echogen.com).
- [7] M.M. Ehsan, M. Awais, S. Lee, S. Salehin, Z. Guan, H. Gurgenci, Potential prospects of supercritical CO<sub>2</sub> power cycles for commercialisation: Applicability, research status, and advancement, *Renewable and Sustainable Energy Reviews*. 172 (2023) 113044. <https://doi.org/https://doi.org/10.1016/j.rser.2022.113044>.

- [8] G.S. Was, P. Ampornrat, G. Gupta, S. Teyssyre, E.A. West, T.R. Allen, K. Sridharan, L. Tan, Y. Chen, X. Ren, C. Pister, Corrosion and stress corrosion cracking in supercritical water, *Journal of Nuclear Materials.* 371 (2007) 176–201. [https://doi.org/https://doi.org/10.1016/j.jnucmat.2007.05.017](https://doi.org/10.1016/j.jnucmat.2007.05.017).
- [9] H.J. Yoon, Y. Ahn, J.I. Lee, Y. Addad, Potential advantages of coupling supercritical CO<sub>2</sub> Brayton cycle to water cooled small and medium size reactor, *Nuclear Engineering and Design.* 245 (2012) 223–232. <https://doi.org/https://doi.org/10.1016/j.nucengdes.2012.01.014>.
- [10] H. Gurgenci, Supercritical CO<sub>2</sub> Cycles Offer Experience Curve Opportunity to CST in Remote Area Markets, *Energy Procedia.* 49 (2014) 1157–1164. <https://doi.org/https://doi.org/10.1016/j.egypro.2014.03.125>.
- [11] S. Lee, G. Yaganegi, D.J. Mee, Z. Guan, H. Gurgenci, Part-load performance prediction model for supercritical CO<sub>2</sub> radial inflow turbines, *Energy Convers Manag.* 235 (2021) 113964. <https://doi.org/https://doi.org/10.1016/j.enconman.2021.113964>.
- [12] Y. Zhang, M. Peng, G. Xia, G. Wang, C. Zhou, Performance analysis of S-CO<sub>2</sub> recompression Brayton cycle based on turbomachinery detailed design, *Nuclear Engineering and Technology.* 52 (2020) 2107–2118. <https://doi.org/10.1016/j.net.2020.02.016>.
- [13] B. Halimi, K.Y. Suh, Computational analysis of supercritical CO<sub>2</sub> Brayton cycle power conversion system for fusion reactor, *Energy Convers Manag.* 63 (2012) 38–43. <https://doi.org/https://doi.org/10.1016/j.enconman.2012.01.028>.
- [14] Z. Guo, Y. Zhao, Y. Zhu, F. Niu, D. Lu, Optimal design of supercritical CO<sub>2</sub> power cycle for next generation nuclear power conversion systems, *Progress in Nuclear Energy.* 108 (2018) 111–121. <https://doi.org/https://doi.org/10.1016/j.pnucene.2018.04.023>.
- [15] M.M. Ehsan, X. Wang, Z. Guan, A.Y. Klimenko, Design and performance study of dry cooling system for 25 MW solar power plant operated with supercritical CO<sub>2</sub> cycle, *International Journal of Thermal Sciences.* 132 (2018) 398–410. <https://doi.org/https://doi.org/10.1016/j.ijthermalsci.2018.06.024>.
- [16] M.A. Reyes-Belmonte, A. Sebastián, M. Romero, J. González-Aguilar, Optimization of a recompression supercritical carbon dioxide cycle for an innovative central receiver solar power plant, *Energy.* 112 (2016) 17–27. <https://doi.org/10.1016/j.energy.2016.06.013>.
- [17] J.D. Osorio, R. Hovsapian, J.C. Ordóñez, Dynamic analysis of concentrated solar supercritical CO<sub>2</sub>-based power generation closed-loop cycle, *Appl Therm Eng.* 93 (2016) 920–934. <https://doi.org/10.1016/j.applthermaleng.2015.10.039>.
- [18] M.M. Ehsan, Z. Guan, H. Gurgenci, A. Klimenko, Feasibility of dry cooling in supercritical CO<sub>2</sub> power cycle in concentrated solar power application: Review and a case study, *Renewable and Sustainable Energy Reviews.* 132 (2020) 110055. <https://doi.org/https://doi.org/10.1016/j.rser.2020.110055>.
- [19] Q. Yu, X. Li, Z. Wang, Q. Zhang, Modeling and dynamic simulation of thermal energy storage system for concentrating solar power plant, *Energy.* 198 (2020). <https://doi.org/10.1016/j.energy.2020.117183>.
- [20] Z. Ma, M.J. Li, K.M. Zhang, F. Yuan, Novel designs of hybrid thermal energy storage system and operation strategies for concentrated solar power plant, *Energy.* 216 (2021). <https://doi.org/10.1016/j.energy.2020.119281>.
- [21] R. Siddiqui, H. Anwar, F. Ullah, R. Ullah, M.A. Rehman, N. Jan, F. Zaman, Power Prediction of Combined Cycle Power Plant (CCPP) Using Machine Learning Algorithm-Based Paradigm, *Wirel Commun Mob Comput.* 2021 (2021). <https://doi.org/10.1155/2021/9966395>.
- [22] P. Tüfekci, Prediction of full load electrical power output of a base load operated combined cycle power plant using machine learning methods, *International Journal of Electrical Power and Energy Systems.* 60 (2014) 126–140. <https://doi.org/10.1016/j.ijepes.2014.02.027>.
- [23] W. Wang, S. Deng, D. Zhao, L. Zhao, S. Lin, M. Chen, Application of machine learning into organic Rankine cycle for prediction and optimization of thermal and exergy efficiency, *Energy Convers Manag.* 210 (2020). <https://doi.org/10.1016/j.enconman.2020.112700>.
- [24] S.M. Besarati, K. Atashkari, A. Jamali, A. Hajiloo, N. Nariman-zadeh, Multi-objective thermodynamic optimization of combined Brayton and inverse Brayton cycles using genetic algorithms, *Energy Convers Manag.* 51 (2010) 212–217. <https://doi.org/10.1016/j.enconman.2009.09.015>.
- [25] M. Saeed, A.S. Berrouk, Y.F. Al Wahedi, M.P. Singh, I.A. Dagga, I. Afgan, Performance enhancement of a C-shaped printed circuit heat exchanger in supercritical CO<sub>2</sub>Brayton cycle: A machine learning-based

- optimization study, Case Studies in Thermal Engineering. 38 (2022). <https://doi.org/10.1016/j.csite.2022.102276>.
- [26] Q. Jin, S. Xia, P. Li, T. Xie, Multi-objective performance optimization of regenerative S-CO<sub>2</sub> Brayton cycle based on neural network prediction, Energy Conversion and Management: X. 14 (2022). <https://doi.org/10.1016/j.ecmx.2022.100203>.
- [27] C.S. Turchi, Z. Ma, T.W. Neises, M.J. Wagner, Thermodynamic study of advanced supercritical carbon dioxide power cycles for concentrating solar power systems, Journal of Solar Energy Engineering, Transactions of the ASME. 135 (2013). <https://doi.org/10.1115/1.4024030>.
- [28] M. Monjurul Ehsan, Z. Guan, A.Y. Klimenko, X. Wang, Design and comparison of direct and indirect cooling system for 25 MW solar power plant operated with supercritical CO<sub>2</sub> cycle, Energy Convers Manag. 168 (2018) 611–628. <https://doi.org/10.1016/j.enconman.2018.04.072>.
- [29] V. Dostal, M.J. Driscoll, P. Hejzlar, N.E. Todreas, ICONE10-22192 A SUPERCRITICAL CO<sub>2</sub> GAS TURBINE POWER CYCLE FOR NEXT-GENERATION NUCLEAR REACTORS, n.d. <http://www.asme.org/about-asme/terms-of-use>.
- [30] M. Monjurul Ehsan, S. Duniam, J. Li, Z. Guan, H. Gurgenci, A. Klimenko, A comprehensive thermal assessment of dry cooled supercritical CO<sub>2</sub> power cycles, Appl Therm Eng. 166 (2020). <https://doi.org/10.1016/j.applthermaleng.2019.114645>.
- [31] M.M. Ehsan, S. Duniam, J. Li, Z. Guan, H. Gurgenci, A. Klimenko, Effect of cooling system design on the performance of the recompression CO<sub>2</sub> cycle for concentrated solar power application, Energy. 180 (2019) 480–494. <https://doi.org/10.1016/j.energy.2019.05.108>.
- [32] Y. Ma, X. Zhang, M. Liu, J. Yan, J. Liu, Proposal and assessment of a novel supercritical CO<sub>2</sub> Brayton cycle integrated with LiBr absorption chiller for concentrated solar power applications, Energy. 148 (2018) 839–854. <https://doi.org/10.1016/j.energy.2018.01.155>.
- [33] V. Zare, M. Hasanzadeh, Energy and exergy analysis of a closed Brayton cycle-based combined cycle for solar power tower plants, Energy Convers Manag. 128 (2016) 227–237. <https://doi.org/10.1016/j.enconman.2016.09.080>.
- [34] Q. Mao, Y. Zhang, Thermal energy storage performance of a three-PCM cascade tank in a high-temperature packed bed system, Renew Energy. 152 (2020) 110–119. <https://doi.org/10.1016/j.renene.2020.01.051>.
- [35] C.S. Turchi, Z. Ma, T.W. Neises, M.J. Wagner, Thermodynamic study of advanced supercritical carbon dioxide power cycles for concentrating solar power systems, Journal of Solar Energy Engineering, Transactions of the ASME. 135 (2013) 1–7. <https://doi.org/10.1115/1.4024030>.
- [36] V. Zare, M. Hasanzadeh, Energy and exergy analysis of a closed Brayton cycle-based combined cycle for solar power tower plants, Energy Convers Manag. 128 (2016) 227–237. <https://doi.org/10.1016/j.enconman.2016.09.080>.
- [37] M. Monjurul Ehsan, Z. Guan, H. Gurgenci, A. Klimenko, Novel design measures for optimizing the yearlong performance of a concentrating solar thermal power plant using thermal storage and a dry-cooled supercritical CO<sub>2</sub> power block, Energy Convers Manag. 216 (2020). <https://doi.org/10.1016/j.enconman.2020.112980>.
- [38] K. Song, F. Yan, T. Ding, L. Gao, S. Lu, A steel property optimization model based on the XGBoost algorithm and improved PSO, Comput Mater Sci. 174 (2020). <https://doi.org/10.1016/j.commatsci.2019.109472>.
- [39] Y. Lu, Y. Li, D. Xie, E. Wei, X. Bao, H. Chen, X. Zhong, The application of improved random forest algorithm on the prediction of electric vehicle charging load, Energies (Basel). 11 (2018). <https://doi.org/10.3390/en11113207>.
- [40] M. Tang, Q. Zhao, S.X. Ding, H. Wu, L. Li, W. Long, B. Huang, An improved lightGBM algorithm for online fault detection of wind turbine gearboxes, Energies (Basel). 13 (2020). <https://doi.org/10.3390/en13040807>.
- [41] G. Ke, Q. Meng, T. Finley, T. Wang, W. Chen, W. Ma, Q. Ye, T.-Y. Liu, LightGBM: A Highly Efficient Gradient Boosting Decision Tree, n.d. <https://github.com/Microsoft/LightGBM>.
- [42] A. Riccardi, F. Fernández-Navarro, S. Carloni, Cost-sensitive AdaBoost algorithm for ordinal regression based on extreme learning machine, IEEE Trans Cybern. 44 (2014) 1898–1909. <https://doi.org/10.1109/TCYB.2014.2299291>.

- [43] Y. Liu, Institute of Electrical and Electronics Engineers, IEEE Circuits and Systems Society, ICNC-FSKD 2017 : 13th International Conference on Natural Computation, Fuzzy Systems and Knowledge Discovery : Guilin, Guangxi, China, 29-31 July, 2017, n.d.
- [44] Z.U. Haq, H. Ullah, M.N.A. Khan, S.R. Naqvi, M. Ahsan, Hydrogen production optimization from sewage sludge supercritical gasification process using machine learning methods integrated with genetic algorithm, Chemical Engineering Research and Design. 184 (2022) 614–626. <https://doi.org/10.1016/j.cherd.2022.06.020>.
- [45] S.M. Alirahmi, M. Rostami, A.H. Farajollahi, Multi-criteria design optimization and thermodynamic analysis of a novel multi-generation energy system for hydrogen, cooling, heating, power, and freshwater, Int J Hydrogen Energy. 45 (2020) 15047–15062. <https://doi.org/10.1016/j.ijhydene.2020.03.235>.
- [46] M. Verma, J. Rajasankar, A thermodynamical approach towards multi-criteria decision making (MCDM), (2015). <https://doi.org/10.1016/j.asoc.2016.10.033>.
- [47] C.H. Chen, A novel multi-criteria decision-making model for building material supplier selection based on entropy-AHP weighted TOPSIS, Entropy. 22 (2020). <https://doi.org/10.3390/e22020259>.
- [48] Q. Jin, S. Xia, P. Li, T. Xie, Multi-objective performance optimization of regenerative S-CO<sub>2</sub> Brayton cycle based on neural network prediction, Energy Conversion and Management: X. 14 (2022). <https://doi.org/10.1016/j.ecmx.2022.100203>.
- [49] P. Mojaver, S. Jafarmadar, S. Khalilarya, A. Chitsaz, Study of synthesis gas composition, exergy assessment, and multi-criteria decision-making analysis of fluidized bed gasifier, Int J Hydrogen Energy. 44 (2019) 27726–27740. <https://doi.org/10.1016/j.ijhydene.2019.08.240>.
- [50] S. mohammad E. Saryazdi, A. Etemad, A. Shafaat, A.M. Bahman, Data-driven performance analysis of a residential building applying artificial neural network (ANN) and multi-objective genetic algorithm (GA), Build Environ. 225 (2022). <https://doi.org/10.1016/j.buildenv.2022.109633>.

#### **Declaration of interests**

The authors declare that they have no known competing financial interests or personal relationships that could have appeared to influence the work reported in this paper.

The authors declare the following financial interests/personal relationships which may be considered as potential competing interests:

#### **Graphical Abstract**

